Politehnica University of Bucharest
Faculty of Aerospace Engineering

Precise Point Positioning Global Navigation Satellite Services Receiver For Space

Doctoral Disertation - Abridged

Drd. Ing. Alexandru Pandele

July, 2021

under the kind supervision of
Prof. Dr. Ing. Adrian-Mihail Stoica

Abstract

Utilizarea serviciilor oferite de sistemele satelitare de navigație globală (GNSS) se extinde la nivelul sateliților și formațiilor satelitare pe orbite joase în jurul Pământului și chiar pentru orbite Lunare. În acest context, această teză de doctorat își propune să avanseze dezvoltarea unui receptor GNSS pentru spațiu, aducându-l de la idee (Nivelul de pregătire tehnologică - TRL 2) la un nivel preliminar de proiectare (TRL 5). Aceasta include o introducere teoretică în domeniul navigării și problemele de poziționare pe care le abordează "Precise Point Positioning" - Poziționarea Punctuală de Precizie. În continuare, va fi prezentată abordarea generală de inginerie a dezvoltării receptorului. Prima fază a implementării acestei abordări este prezentată în ultimele trei capitole, începând cu definirea cerințelor, proiectarea preliminară și testarea componentelor critice preliminare. Teza este completată cu Concluzii.

Cuvinte cheie: GNSS, PPP, subsisteme satelitare, testare tehnologie spațială

The use of services provided by global navigation satellite systems (GNSS) extends to satellites and satellite formations in low orbits around the Earth and even to lunar orbits. In this context, this doctoral thesis aims to advance the development of a space GNSS receiver, bringing it from idea (Technological Readiness Level - TRL 2) to a preliminary design level (TRL 5). This includes a theoretical introduction to navigation and positioning issues that "Precise Point Positioning" addresses. Next, the general engineering approach to receiver development will be presented. The first phase of implementing this approach is presented in the last three chapters, starting with the definition of requirements, preliminary design and testing of preliminary critical components. The thesis is completed with Conclusions.

Keywords: GNSS, PPP, satellite subsystems, space technology testing

Contents

1 Introduction

Satellite formations are coming of age and are being used on larger and larger scales in a variety of missions. In view of more complex operations, higher accuracy positioning and maneuvering are required for the members of the formations. Positioning solutions based on Global Navigation Satellite Systems (GNSS) such as the American Global Positioning System (GPS) or the European GALILEO have the potential to answer the stringent requirements imposed by satellite formations. This is especially true when GNSS signals are augmented by corrections computed with the help of ground based monitoring networks.

This thesis proposes to complete the first stages of the development of such a receiver, bringing it from application idea (Technology Readiness Level - TRL 2) to a preliminary design level (TRL 5). This shall include a theoretical introduction in the subject of navigation and the positioning problems that Precise Point Positioning is addressing. Following that, the overall engineering approach of the receiver development shall be presented. The first phase of the implementation of this approach is presented in the last three chapters, starting with the definition of requirements, the preliminary design and testing of the preliminary critical components. The thesis is completed with Conclusions. The original contribution of this thesis is concentrated in the architecture and realization of the PPP GNSS receiver for space, aiming for high precision, high reliability and low cost.

The objectives of this thesis are:

- presentation of the underlying theory for precise positioning and navigation based on the Global Navigation Satellite Systems (GNSS);
- definition of an engineering approach for the development of a PPP GNSS receiver for space;
- requirements identification and consolidation for a PPP GNSS receiver for space;
- identification, development and testing of critical features such as an artificial neural network augmented orbit propagator and a fault detection, identification and recovery mechanism;
- identification and testing of preliminary components.

It is proposed to develop OrbFIX [1], a low-cost, COTS-based, Precise Point Positioning, multi-constellation, multi-frequency GNSS receiver for micro and small satellites, allowing ≤10 cm positioning accuracy on a low Earth orbit. Additionally, the product integrates orbit determination algorithms and two low-power positioning modes that take advantage of a precise orbit propagator and of an on-board neural network. These features increase the positioning accuracy when PPP corrections are not available, or a smaller power consumption is required.

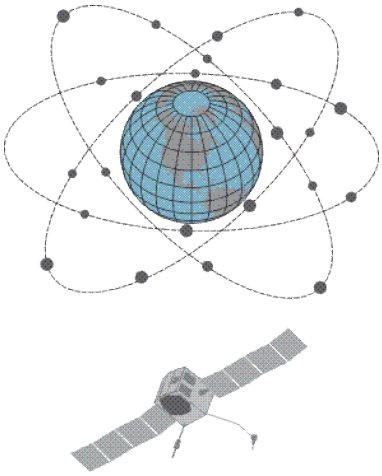

Figure 1.1: GALILEO GNSS orbital planes and typical satellite (https://www.e-education.psu.edu/geog862/print/l10.html).

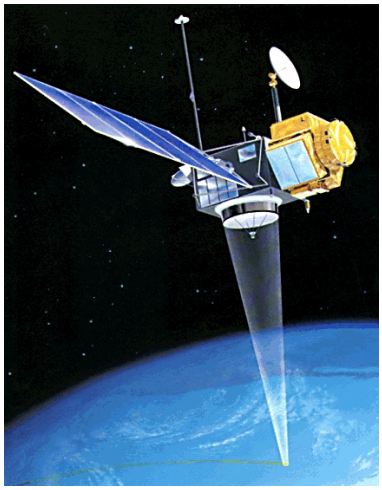

Figure 1.2: Topex/Poseidon (NASA/CNES) mission, launched in 1992 - one of the first satellites to use GNSS positioning (wikimedia.org).

Global Navigation Satellite Systems - Basic Principles

2

Navigation is defined by the Oxford Dictionary[2] as *the process or activity of accurately ascertaining one's position and planning and following a route*. This activity was practiced by humans since the dawn of time, first on land, then on water, much later in the air and nowadays also in space.

Land navigation benefits greatly from relief and vegetation features that may constitute a good reference for the land traveler and even for the air traveler flying over land. However, open sea navigation or navigation over land with little distinguishable features require alternative references. At the beginning, these were celestial. The apparent solar movement provided navigation clues during the day, while the stars helped navigators during the night [3]. The invention of the compass [4] brought the added value of using another reference system, the Earth's magnetic field, and a reduced dependency on the whims of the weather. However, celestial and magnetic navigation could only be used for a relatively precise determination of latitude, navigators determining their longitude only by reference to time and speed of traveling. It was only with the invention of precise chronometers [5] that navigators were finally able to determine their position with an unprecedented accuracy of a few tens of kilometers. From this status, navigation improved only marginally, mostly in the precision of the instruments it used (better chronometer, better speed determination, better compasses, etc), until the advent of radio navigation at the end of the XIXth century[6].

Figure 2.1: A mariner's astrolabe measures the angle of the Sun or a star above the horizontal line of reference (*source:* `https://timeandnavigation.si.edu`)

Figure 2.2: Chronometer (*source:* `https://timeandnavigation.si.edu`)

2.1 Satellite navigation

The principles of radio navigation were used as early as the end of the XIX-th century and have evolved by responding to the needs of maritime navigation and of the young field of aeronautics, and by taking advantage of the technological advances of telecommunication engineering, especially during and in the wake of the two World Wars. A different type of war, the Cold one, and the Space Race it engendered brought the next leap in radio navigation by introducing satellites as the sources of ranging signals.

Engineers of the United States Naval Center for Space Technology overcame their awe following the Soviet launch of Sputnik-1 in 1957 and realized that they can determine the first satellite's orbit based on the Doppler effect [7]. They went one step further and concluded that satellites could be used for the positioning of ground receivers. Three years later, the first TRANSIT satellite was launched on a polar orbit, followed in the next years by five more [8]. The TRANSIT constellation became the first satellite navigation system. In 1978 was launched the first Navigations System with Timing and Ranging (NAVSTAR) satellite [9]. This shall become fully operational in 1993, with the availability of the complete 24

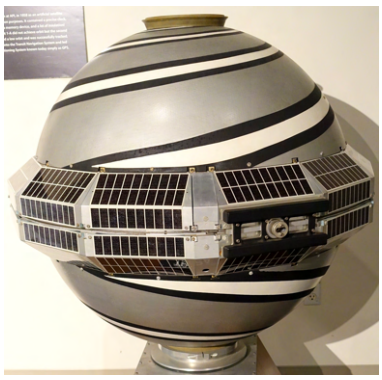

Figure 2.3: Transit-2A navigation satellite model (*source:* `https://commons.wikimedia.org`)

(a) (b) (c) (d)

Figure 2.4: Four ways to know where you are: (a) GPS; (b) GLONASS; (c) GALILEO; (d) BeiDou

satellite constellation. It is better known now as the Global Positioning Systems (GPS).

While pioneering the field of navigation satellites, the USA are not monopolizing it. The first Soviet, then Russian experiments concluded in the development of the GLONASS - Globalnaya navigatsionnaya sputnikovaya sistema or the Global Navigation Satellite System, that reached full operation in 1995 [10]. European efforts led to the deployment of the GALILEO constellation [11], aiming to be completed in 2020, at the same time with the Chinese BeiDou (from the Chinese name of the Ursa Major constellation) navigation satellite system [12]. Local area satellite positioning systems have been deployed also by Japan (MSAS)[13] and India (IRNSS)[14].

2.1.1 GNSS Architecture

The architecture of a Global Navigation Satellite System is comprised of two main elements: the infrastructure and the signals. These elements shall be briefly described in the following sections, with an accent on the GPS architecture.

2.1.1.1 GNSS Infrastructure

GNSS infrastructure consists of three main segments: the satellites or the space segment, the control or the ground segment and the user segment.

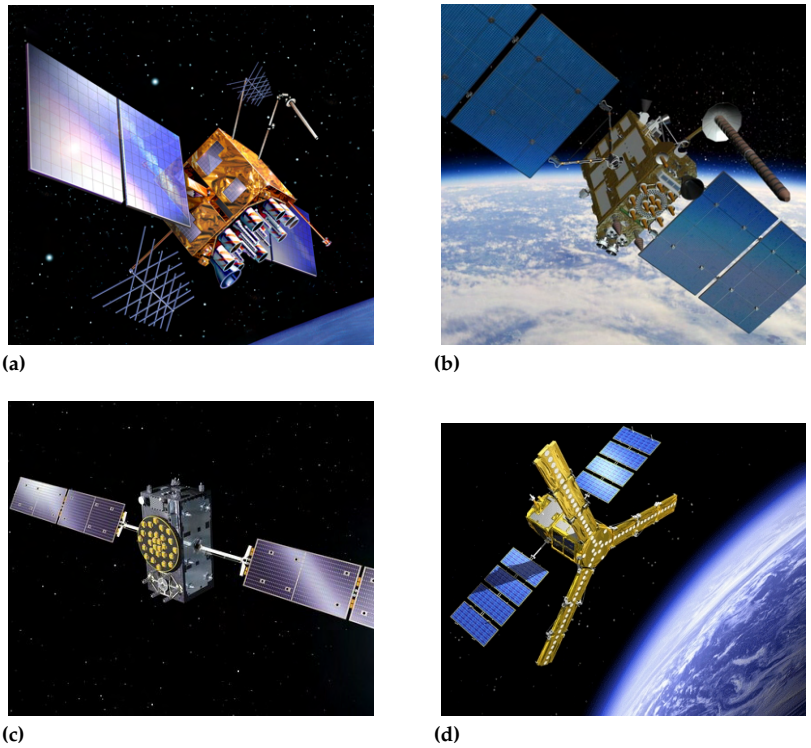

(a) (b) (c) (d)

Figure 2.5: Roaming in space: (a) GPS Block II; (b) GLONASS-K; (c) GALILEO FOC; (d) BeiDou

2.1.1.1.1 Space Segment In order to provide positioning services worldwide, GNSS space segments are deployed in various constellation configurations. They play the role of the beacons.

The nominal GPS constellation includes 24 satellite vehicles (SV) arranged in four slots on each of six equally spaced orbital planes [15]. GLONASS provides its nominal services using 24 satellites and 2 spares. Similarly, three planes are used for the nominal, 27 operational and 3 spares, GALILEO satellites. BeiDou GNSS configuration is rather complex, including 27 Medium Earth Orbit (MEO) satellites, 3 satellites on an Inclined Geosynchronous Satellite Orbit (IGSO) and 5 GEOstationary (GEO) satellites [16].

2.1.1.1.2 Control Segment The control segment is responsible with the operation of the GNSS. Its main activity consists in controlling and maintaining the space segment and in insuring that all elements are in place for accurate and reliable positioning. This includes predicting the satellites' orbit coordinates (ephemeris) and clock evolution, generate a stable, (atomic) clock reference and provide timely navigation messages for all constellation satellites.

2.1.1.1.3 User Segment The user segment of the GNSS is composed by a wide range of receivers. They are essentially being used for positioning and navigation on land, on water, in the air and in space, but also as time references (e.g. for communication networks). Irrespective of their usage, GNSS receivers have a generally common architecture as presented in figure 2.6. An antenna tuned in the GNSS frequencies acquires the analog signal which is amplified by a Low Noise Amplifier (LNA) before being

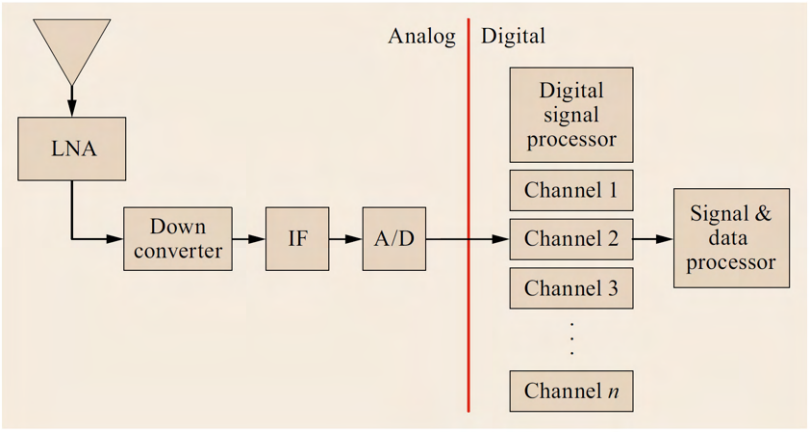

Figure 2.6: Basic digital receiver architecture (*source: [17]*)

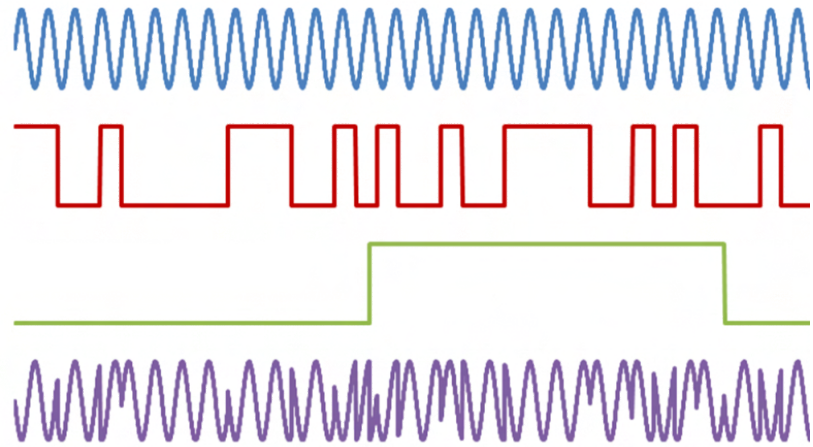

Figure 2.7: Main GPS L1 C/A components: the L1 carrier at 1575.42 MHz (blue); C/A PRN at 1.023 MHz with 1 µs chip duration and a period of 1023 chips (red); navigation information at 50 Hz (green); composition change of phase (violet) (*source: https://gssc.esa.int/navipedia/index.php/GNSS_signal*)

down converted to an Intermediate Frequency and fed to an Analog-to-Digital (A/D) converter. A digital signal processor (DSP) extracts the useful information from the digitized signal. A signal and data processor converts this information in pseudoranges and other observables, and computes the position.

2.1.1.2 GNSS Signals

In figure 2.7 the main components of the GPS L1 C/A signal are presented. A *carrier* frequency in the L band is used to transmit a *pseudo-random code* (PRN) which is specific to each satellite and is a sequence of 1023 chips (sequence of 1's and 0's). This code is known to the receiver, 32 PRN's being defined for the GPS constellation. The PRN is used to lock on the satellite signal and to determine the time delay between the transmission and the reception. On top of the carrier and the PRN code, a *navigation message* is being sent at a frequency of 50 Hz. The navigation message includes binary coded information describing the orbit of the satellite (satellite ephemeris), the satellite clock bias, satellite health status, the constellation almanac and other data. The almanac is a set of ephemeris for all constellation satellites, recorded with lower accuracy, which allows the receiver to reduce the search for satellites to only those that are in view.

Figure 2.8 summarizes the carrier frequencies that are being used by

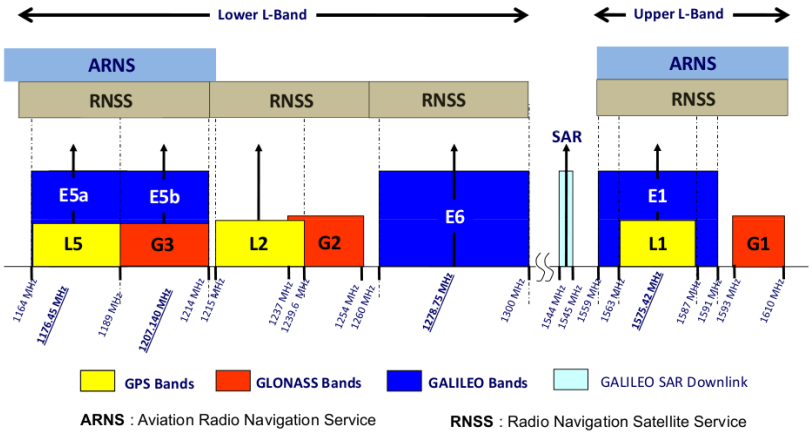

Figure 2.8: Main navigational frequency bands (*source: [18]*)

GPS, GALILEO and GLONASS. BeiDou is using a spectrum similar to GALILEO, with a slightly different center frequency for B3 (equivalent of E6). At first sight, the choice of frequencies is difficult to understand as all systems use the same carriers for their signals, seeming to interfere with each other.

Common carrier frequencies is an interoperability strategy of GNSS that allows receiver manufacturers to use the same hardware no matter the supported system. A GPS L1 receiver requires only a firmware update in order to become a GALILEO E1 receiver.

GNSS Positioning 3

3.1 GNSS Measurements

The main information that can be extracted from the GNSS signal is the time necessary for it to travel between the satellite antenna and the receiver antenna. Knowing the signals travels with the speed of light (c), results that the *apparent* distance between the two antennas is:

$$R = c\Delta T \tag{3.1}$$

We discuss about apparent distance, or **pseudorange**, to emphasize the fact that it includes various effects that need to be modeled and removed in order to get closer to the absolute distance.

Equation 3.1 assumes no synchronization error between the satellite and the receiver. Considering synchronization, the equation becomes:

$$R = c(\Delta T - \delta t) \tag{3.2}$$

where the δt term covers the synchronization errors between the satellite's and receiver's clocks and the GNSS reference clock.

The pseudorange defined in equation 3.2 includes, besides the real, geometric distance between the satellite and the receiver antennas, a series of errors due to various phenomena affecting the radio signal transmission. These phenomena and the magnitude of errors they induce are summarized in figure 3.1.

It is obvious that there is a direct relationship between distance and time. This implies a difficulty in discriminating between synchronization/clock errors and distance/orbit positioning errors. To better grasp the time/distance relationship, it is to be noted that 1 ns represents approximately 30 cm and 3.3 ns represents approximately 1 m.

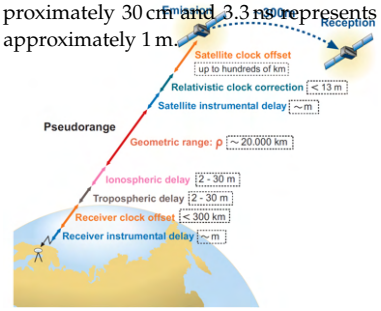

Figure 3.1: Pseudorange measurement contents (*source: [18]*)

Equation 3.2 can then be re-written as [18]

$$R = \rho + c(dt_{rec} - dt_{sat}) + T + I + K_{rec} - K_{sat} + M + \epsilon \tag{3.3}$$

where:

- ρ is the geometric range between the satellite and receiver antennas;
- dt_{rec} and dt_{sat} are the synchronization errors of the receiver and satellite clocks with respect to the GNSS reference clock;
- T is the tropospheric delay;
- I is the ionospheric delay;
- K_{rec} and K_{sat} are the instrumental delays at receiver and satellite level;
- M is the multipath error due to the signal being received not on a direct, "line of sight" path, but on path including reflections on various surfaces, usually in the immediate vicinity of the receiver;
- ϵ is the receiver noise.

3.2 Equations

The equations used for the PPP technique are described in [17]. A GNSS receiver measures the time in which the GNSS signal propagates from

a satellite to the receiver. The following basic equation can be used to compute the range from the satellite to the receiver, using the measured time and the speed of light:

$$\rho_r^s(t) = c\tau_r^s \tag{3.4}$$

where: s denotes the satellite antenna;
$r$denotes the receiver antenna;
ρ_r^s represents the geometrical range;
c is the speed of light; and
τ_r^s represents the time measured by the GNSS receiver.

However, this ideal equation does not take into consideration the receiver and satellite clock errors. In this case, the range measurements biased by the clock errors are denoted pseudoranges and the equation becomes:

$$p_r^s = \rho_r^s + c(dt_r - dt^s) \tag{3.5}$$

where p_r^s is the pseudorange, dt_r represents the receiver clock error and dt^s represents the satellite clock error.

The satellite clock errors are monitored by GNSS operators and correction parameters are sent to the satellites. The satellites than broadcast the clock corrections in the navigation message. On the other hand, the receiver clock error is still unknown. Adding also the coordinates of the receiver antenna position (x_r, y_r, z_r), there are four unknown terms in the pseudorange observation equation. They can be determined by using at least four simultaneous pseudoranges. Nevertheless, there are additional factors that should be taken into consideration, such as the ionospheric and tropospheric delays, receiver noise and multipath. These errors can be modelled using an increased number of GNSS satellites. The receiver coordinates and clock offset can then be calculated using nonlinear least-squares estimation. Considering these additional errors, the pseudorange measurement can be calculated using the following expression:

$$p_{rj}^s(t) = \rho_r^s(t) + \xi_{rj}^s(t) + c(d_{rj} - d_j^s) + c(dt_r(t) - dt^s(t) + \delta t^{rel}(t)) + I_{rj}^s(t) + T_r^s(t) + e_{rj}^s(t) \tag{3.6}$$

where
j is used to identify between different signals from the same satellite;
ξ_r^s contains the correction for the phase center offsets between the transmitting and the receiving antennas and the contribution of code-phase patterns;
d_r and d^s represent the instrumental delays of the receiver and of the satellite;
$\delta t^{rel} = \delta t_{stc}^{rel} - \delta t_{clk}^{rel}$ is a term that combines the relativistic signal delay due to space-time curvature and the relativistic clock correction;
I_r^s represents the ionospheric delay;
T_r^s represents the tropospheric delay; and
e_r^s is used to denote other errors, such as receiver noise and multipath.

In a similar manner, one can define the observation equation for the carrier-phase measurements:

$$\phi^s_{rj}(t) = \rho^s_r(t) + \zeta^s_{rj}(t) + c(\delta_{rj} - \delta^s_j) + c(dt_r(t) - dt^s(t) + \delta t^{rel}(t)) - I^s_{rj}(t) + T^s_r(t) + \lambda_j(\omega^s_r(t) + N^s_{rj}) + \epsilon^s_{rj}(t) \quad (3.7)$$

where
ϕ^s_r is the carrier-phase measurement;
ζ^s_r represents the phase center offset correction;
δ_r and δ^s represent the receiver and satellite instrumental delays;
ω^s_r is the phase wind-up correction, which is used to identify changes in the measured phase if rotations of the antenna occur;
N^s_r denotes the unknown integer number of cycles; λ is the wavelength; and
ϵ^s_r represents the residual error term, containing the receiver noise and multipath.

The geometric range, clock offsets and tropospheric error are identical in both equations. The ionospheric delay has a positive sign for the pseudorange and a negative sign for the carrier-phase measurements. Also, the ionospheric delay depends on the frequency of the observations because the ionosphere is a dispersive medium and different frequency observations are affected in different ways. Therefore, using a combination of at least two frequencies, it is possible to almost completely remove these ionospheric errors.

The linear combinations of pseudorange and carrier-phase GNSS observations can be expressed using the following equation:

$$o_(r,c)^s(t) = \sum_{j=1}^{n}(\alpha_j \phi^s_{r,j}(t) + \beta_j p^s_{r,j}(t)) \quad (3.8)$$

where
$o^s_{r,c}$ denotes the combined observable;
n is the number of different signals available;
α_j represents the coefficient used to scale the carrier-phase observations; and
β_j represents the coefficient used to scale the pseudorange observations.

By replacing in this expression the equations for the carrier-phase and pseudorange measurements, two scaling factors can be introduced, allowing some controllability on the equation parameters. The first factor allows the control of the geometric range, clock offsets and tropospheric delay:

$$\sum_{j=1}^{n}(\alpha_j + \beta_j) = h_1 \quad (3.9)$$

If $h_1 = 1$, the combination is called geometry-preserving. If $h_1 = 0$, then the combination is called geometry-free. In the same manner, the

first-order ionospheric delay can be controlled using:

$$-\sum_{j=1}^{n}(\alpha_j+\beta_j)\frac{f_1^2}{f_2^2}=h_2 \tag{3.10}$$

A scaling factor $h_2 = 0$ creates an ionosphere-free combination.

A dual frequency ionosphere-free combination uses two carrier-phase observations and two pseudoranges with different frequencies. The objective is to preserve the geometry while eliminating the ionosphere. Therefore, the scaling factors are $h_1 = 1$ and $h_2 = 0$. Denoting the two frequencies f_A and f_B, the β coefficients corresponding to each frequency can be calculated as:

$$\beta_A = 1-\beta_B = \frac{f_A^2}{f_A^2-f_B^2} \tag{3.11}$$

Therefore, the ionosphere-free pseudorange combination can be expressed as follows, using the pseudoranges for both frequencies:

$$p_{r,IF}^s = \frac{f_A^2}{f_A^2-f_B^2}p_{r,A}^s - \frac{f_B^2}{f_A^2-f_B^2}p_{r,B}^s \tag{3.12}$$

Similarly, the ionosphere-free carrier-phase combination is characterized by the following equation.

$$\phi_{r,IF}^s = \frac{f_A^2}{f_A^2-f_B^2}\phi_{r,A}^s - \frac{f_B^2}{f_A^2-f_B^2}\phi_{r,B}^s \tag{3.13}$$

The wavelength of the ionosphere-free carrier phase combination has the following form:

$$\lambda_I F = \frac{\lambda_A\lambda_B}{i_A\lambda_B + i_B\lambda_A} \tag{3.14}$$

where
λ_A and λ_B are the wavelengths for A and B frequencies and
i_A and i_B are the integer-phase coefficients for A and B frequencies.

Based on these equations, the precise point positioning method uses both pseudoranges and carrier-phase measurements in order to obtain more accurate results. The ionospheric-free dual frequency combination of GNSS pseudorange and carrier-phase measurements is characterized by the following equations:

$$p_{r,IF}^s = \rho_r^s + c(dt_r - dt^s) + T_r^s + e_{IF} \tag{3.15}$$

$$\phi_{r,IF}^s = \rho_r^s + c(dt_r - dt^s) + T_r^s + \lambda_{IF}A_{IF} + \epsilon_{IF} \tag{3.16}$$

where
A_{IF} represents the non-integer ambiguity of the ionosphere-free carrier-phase combination; and
e_{IF} and ϵ_{IF} are the measurement noise parameters.

The unknown terms in the precise point positioning method are the coordinates of the receiver position, the receiver clock, the zenith tropospheric delay and the non-integer ionosphere-free carrier-phase ambiguities. When using PPP, the estimates of these parameters are consistent with the global reference system inferred by the fixed global GNSS orbit/ click solutions. Even though the PPP applications usually use the GPS L1 and L2 frequency, the method described in this chapter can also be used with other frequency combinations, including the L5 and E5 frequencies.

3.3 Multi-frequency multi-constellation PPP

Although it was initially designed for dual frequency GPS observation, the precise point positioning method can be used for various signals and constellations. The additional signals can enhance the PPP performance, but they also bring new challenges that have to be addressed. For example, the standards used for GPS and GLONASS regarding the use of auxiliary products, such as the GNSS orbits and clocks, should be updated to include the new signals and constellations. The ionosphere-free dual frequency pseudorange and carrier phase observations combinations can be computed using any GNSS constellation or combination of constellations. In the case of combining signals from different constellations, an intersystem bias has to be estimated for all except one constellation. The bias is assumed to be constant over the processing arc and its role is to compensate for possible constellation-specific receiver biases and system time offsets. Moreover, if the used signals are different than the ones used in the clock product, satellite-specific differential code biases have to be applied.

When selecting the signals to be used, one has to take into consideration the signal availability (i.e. the selected signal should be broadcasted by all satellites in the constellation), the signal characteristics, such as multipath resistance and carrier-to-noise ratio, and the clock product that will be used. In addition, the noise of the ionosphere-free combination will be minimized by choosing widely spaced signals. This means that the combinations of GPS frequencies L1/L2 and L1/L5 are good options, while the L2/L5 combination is not. Studies have shown that multi-constellation PPP solutions provide increased robustness, a better convergence time and improved accuracy. They are particularly useful in constrained environments, in which the number of visible satellites is lower.

The use of more than two frequencies for PPP processing can be approached in different ways [19]. One option is to process multiple ionosphere-free dual frequency combinations, taking into consideration the correlation induced by using the same measurement in the combined observations. An example of such a combination is represented by GPS L1/L2 and L1/L5 combination. Another approach is to use uncombined code and carrier phase measurements for each of

the available frequencies, while introducing additional estimation parameters such as the ionospheric slant delays. This method provides the benefit of using the simplest observational variance matrix, while further model strengthening can be performed using all the available parameters.

Engineering approach 4

The goal of the thesis is to advance the design, assembling and testing of two prototype PPP space GNSS receiver units. These shall be able to provide sub-decimeter positioning on LEO, shall be targeting a 95% availability and shall provide improved, low-power positioning methods. One of them shall be tested at qualification level and the other at acceptance level, ready to be integrated in an in-orbit-demonstration (IOD) mission. The name chosen for the receivers, OrbFIX, is derived from its purpose: determining with high accuracy the orbital position of a satellite. The OrbFIX development shall be done in view of a series production. The technical objectives to be met derive directly from the application of the development and are:

- Identify and test a suitable COTS GNSS receiver as the OrbFIX backbone;
- Preliminary design and test of the low-power positioning and orbit determination modes;
- Design the PPP OrbFIX space GNSS receiver;
- Assemble, integrate and test two OrbFix prototype units;
- Consolidate mission requirements for demonstrating the hardware in space.

The technical objectives listed above are both necessary and sufficient to develop OrbFIX, a COTS (Components Off The Shelf) based GNSS receiver integrating precise point positioning and precise orbit determination (POD) algorithms for nano and micro satellites on LEO.

OrbFIX is based on COTS components, thus a market analysis and preliminary evaluation is necessary to select the most suitable COTS GNSS receiver and microcontroller. These components shall be selected such that they shall fulfill the OrbFIX requirements.

While PPP and POD are a step forward and enabler technologies in the micro and nano satellite market, one needs to consider one of the specifics of this market which is the limited amount of power available on board. This led to considering the integration of two low-power modes, both based on artificial neural networks (ANN). These positioning modes shall be implemented and tested prior to their integration in the final OrbFIX design.

Having gathered the main hardware components, the OrbFIX design is the next logical step. This shall take into consideration availability issues as well as the methods for acquiring PPP corrections and shall result in a preliminary design.

Fulfilling the last two technical objectives shall complete the development of a subsystem prototype that is ready to be tested in real conditions and that, following successful tests, becomes a competitive product on a developing market

4.1 Approach overview

The proposed approach for reaching the technical objectives is very pragmatic and derives from the CubeSat COTS philosophy. It involves the identification of a commercial-off-the-shelf GNSS receiver developed originally for ground utilization. This receiver needs to be easily customized to fit the basic requirements of a GNSS space receiver and allow the implementation of Precise Orbit Determination (POD) algorithms.

OrbFIX shall integrate two low-power positioning modes that are considered essential for micro and nano satellites which are, in general, very limited from the point of view of available power [20]. Both modes make use of neural networks, aiming to reduce computation power and take advantage of the ANN's capability to be trained for each mission[21]. Either on board or on the ground, PPP can be used to determine a precise orbit for the satellite. This precise orbit may be used by mission operators to train two ANNs that are fed with the corresponding GNSS measurements and/or the output of an orbit propagator. The trained ANN are then uploaded on-board and are periodically updated from ground.

4.2 COTS hardware selection and testing

After consolidating OrbFIX requirements, the project is continued by reviewing the potential COTS components and trading them off for the OrbFIX receiver. Several design architectures shall be assessed, starting from the one pictured in Figure 4.1. In this design, a rad-hardened COTS MCU, such as ATmegaS128 or the more powerful AT7913E from Microchip, shall control the operation of the COTS GNSS receiver. The MCU shall also be responsible with the implementation of the PPP algorithm and the precise orbit determination (POD). When PPP correction data is not available, the neural network enhanced lightweight orbit propagator is also ran on the MCU. Communication with the satellite bus is planned to be available on UART and CAN.

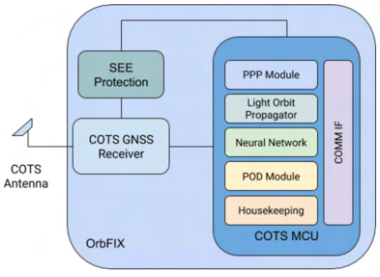

Figure 4.1: Preliminary OrbFIX system diagram

4.3 Single Event Effects (SEE) and Total Ionizing Dose (TID) protection

Single Event Effects are malfunctions of electronic components (microcontrollers, memory, etc.) caused by single, energetic particles, typically galactic cosmic rays (GCR). Total Ionizing Dose is the amount of protons, electrons and *brensstrahlung* X-ray dose produced by the radiation environment which is an indicative of the cumulative degrading effects on electronics [22]. Independent of the chosen COTS receiver, OrbFIX shall focus on the radiation protection design in line with requirements from the European Space Agency's ECSS-E-ST-10-12C standard and the ECSS-Q-HB-60-02A recommendations. This includes the estimated energetic particle environment for LEO orbits, the estimated TID and use worst case estimates for single event effects. The calculated environment will be used to assess irradiation tests performed on the hardware chosen

for the receiver. The design of OrbFIX will take into account radiation hardening to a sufficient level for the target availability[23].

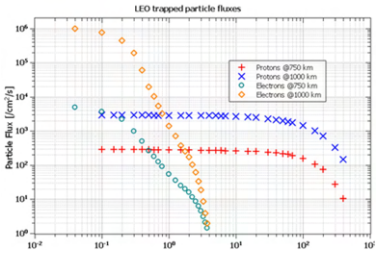

Figure 4.2: Trapped particle radiation fluxes for circular orbits *source:* `https://www.spenvis.oma.be/`

4.4 Low power positioning modes

OrbFIX integrates low-power positioning modes based on a lightweight orbit propagator (OP) [24] [25] [26]. The OP feeds an Artificial Neural Network (ANN) [27] that, when properly trained, applies vital corrections to its input stream to obtain accurate positions. Following this logic, the application is devised in two levels, namely L0 and L1. The L0 consists of the orbital propagator that estimates the position and velocity of the satellite. The computed data is filtered through a trained ANN designed to output the accurate position. A functional decomposition of L0 is depicted in figure 4.3.

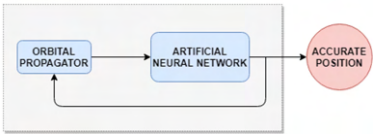

Figure 4.3: L0 functional blocks

Although the difference between the real position and the estimated one is relatively small at the beginning of computations, the error rapidly increases in time. A feasible solution is to reinitialize the orbital propagator with the accurate positions; the frequency of the re-initialization is strongly dependent on the rate at which the errors accumulate.

The L1 is build upon L0. A second ANN is trained with the purpose of receiving input from both the orbital propagator and the GNSS device, as illustrated in figure 4.4. The purpose of L1 is to improve the accuracy of measured positions and velocities. The use of an orbital propagator is justifiable because it inherently encapsulates a physical model that the satellite obeys. Along with the measured positions and velocities, the data is processed by the ANN which outputs an accurate position. As with L0, the orbital propagator must be reinitialized when the accumulated errors can no longer be compensated.

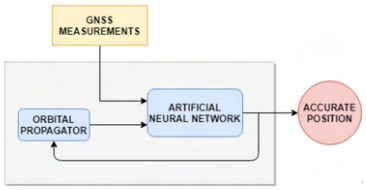

Figure 4.4: L1 functional blocks

4.5 Precise Point Positioning

Precise point positioning (PPP) was first introduced in 1997 by [28]. Unlike relative positioning, PPP uses undifferenced pseudorange and carrier-phase observations, and doesn't need simultaneous observations at two stations. Instead, PPP relies on precise orbits and clocks that replace the ones being broadcast by the satellite. In figure 4.5 it can be seen that the difference between precise and broadcast orbits and clocks is a significant positioning error source, in the order of 4 meters for GPS and in the order of 2 meters for Galileo. However, compensating for this error is not sufficient to increase positioning accuracy to 10 cm or less. This is achieved by considering carrier-phase measurements, which in turn bring the added difficulty of determining the initial phase ambiguity unknowns and imply a longer convergence time for the PPP solution (up to 15 minutes or more).

The proposed navigation Kalman filter in charge of the computation of the PVT solution will estimate the carrier-phase ambiguities are estimated as real numbers in what is called the floating ambiguities. The changes in the GNSS satellite geometry will help to decorrelate (separate) the

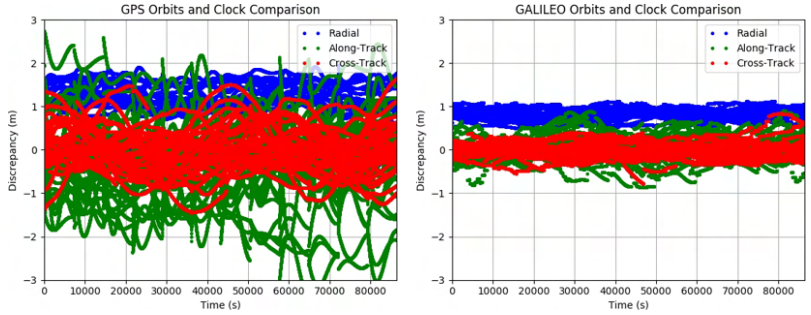

(a) **(b)**

Figure 4.5: Broadcast orbits and clocks errors for GPS (a) and Galileo (b)

floated ambiguities from the other parameters being estimated in the navigation filter (position, receiver clock, wind-up).

4.6 Review and implementation of standards

As the market primarily targeted by OrbFIX is represented by micro and nano satellites following the Cubesat standard, this shall guide its design. From a subsystem's point of view, such as the GNSS receiver, the Cubesat Design Specification [29] has limited effect as the document is primarily meant for satellite developers. The overall subsystem envelope should be smaller than the 100 x 100 x 100 mm in the standard. Practically the form factor for every internal subsystem must match the PC/104 specification as most of the CubeSat subsystems use this footprint of approximately 96 x 90 mm.

4.7 Technical feasibility

Although minimizing some of the development and costs risks, the COTS utilization approach of the complete activity has inherent issues associated with the qualification for space of components and achieving the targeted reliability of the integrated system. The components to be traded off have, at least in part, demonstrated functionality in a high radiation environment. However, the demonstrations are not consistent, and they certainly don't cover the integrated product, therefore the need for a de-risk activity. Several risks have been identified in the development process:

1. Unavailability of COTS receiver meeting all criteria.
   Impact/Likelihood: High/Unlikely
   Mitigation: Several candidate products have been identified. Required features could be implemented by the secondary processing unit if implementation in the receiver is not possible.
2. Radiation hardening partial failure
   Impact/Likelihood: High/Possible
   Mitigation: A COTS receiver with partial inherent radiation tolerance is the main candidate for the receiver. Parts for which radiation hardened variants exist will be better graded in the design trade-off. The hardening process is expected to include both shielding for TID and monitoring for SEE integrated in the device.

Requirements 5

ORBFIX DEVELOPMENT is done based on a set of requirements. This was initially reduced to essentials (such as maximum power consumption, size, etc). However, the initial set needs to be extended in order to guide the development and help eventual design trade-offs. OrbFIX aims to be a low-cost, COTS-based, Precise Point Positioning, multi-constellation, multi-frequency GNSS receiver for micro and small satellites, allowing ≤10 cm positioning accuracy on a low Earth orbit. These objectives are flown down in requirements grouped as General, Functional, Physical, Environmental and Testing.

5.1 Requirements summary

Table 5.1: OrbFIX GNSS receiver basic requirements

Req. Id.	Subject of the requirement	Requirement
REQ-10	Volume	< 1 Unit CubeSat
REQ-20	Mass	≤300 g
REQ-30	Maximum power	≤4 W
REQ-40	Average power	≤2 W
REQ-50	Operational temperature	[-30, +60]°C
REQ-60	Storage temperature	[-40, +70]°C
REQ-70	Supply voltage	3.3 V and/or 5 V
REQ-80	Interfaces	CAN/I2C/SPI
REQ-90	Constellations	GPS & Galileo
REQ-100	Frequencies	L1/E1 & L5/E5a
REQ-110	PPP corrections source	Geostationary satellite and/or ground station connection
REQ-120	Tracked satellites	≥24

Design 6

6.1 Design options

Two alternative approaches have been identified that deal with one of the main features of the receiver: the delivery of the precise point positioning corrections.

1. Independent geostationary delivery of corrections
   In this approach, a dedicated radio front-end is combined with a software defined radio (SDR) in order to acquire and demodulate PPP corrections provided via GEO satellites signals by a commercial provider. Preliminary discussions with Fugro, a well-known, global provider of PPP corrections, have suggested both the interest and the willingness to support such an approach, with an architecture described in the figure 6.1
2. Receiver dependent PPP
   In this case, the PPP corrections delivered via a geostationary satellite shall be decoded directly by the GNSS receiver, which shall in turn provide a PPP solution. The corresponding architecture is presented in figure 6.2.

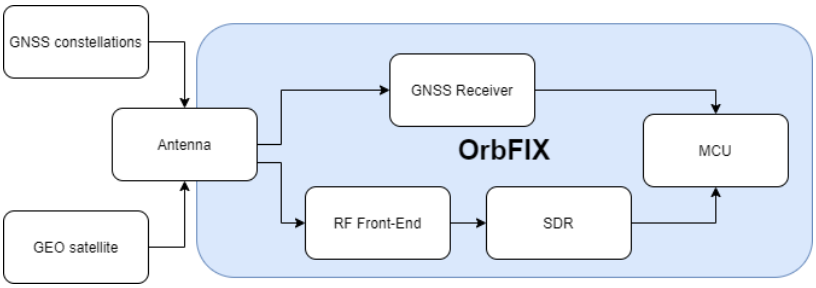

Figure 6.1: Architecture for independent correction delivery

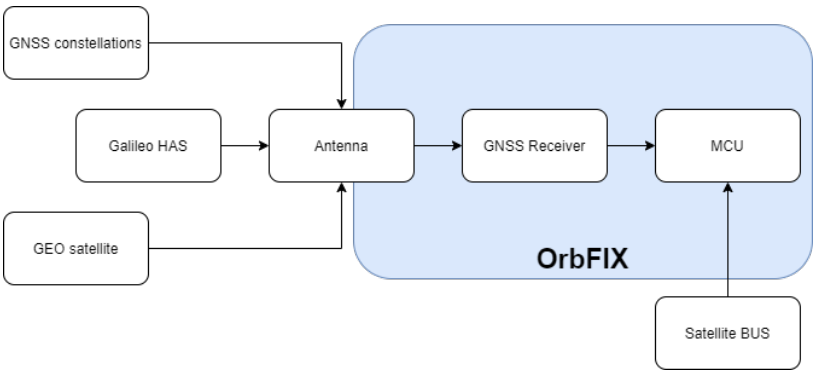

Figure 6.2: Architecture for receiver dependent corrections delivery

6.1.1 Preliminary design choice

Between the two architectures presented in paragraphs Independent geostationary delivery of corrections and Receiver dependent PPP, the

preliminary design choice is Receiver dependent PPP The reduced power requirements and dimensions make this design most suitable for fulfilling the OrbFIX requirements. On the other hand, the receiver dependent PPP design may be developed such that an extension board could allow the implementation of the independent geostationary delivery of corrections. Such an add-on will give complete flexibility for the final product, the trade-off between using geostationary corrections and low power consumption being left to the customer.

6.2 Software architecture

OrbFIX software architecture is driven by the requirements in section 3 and is summarized in the fig. 6.3. The software shall be implemented on

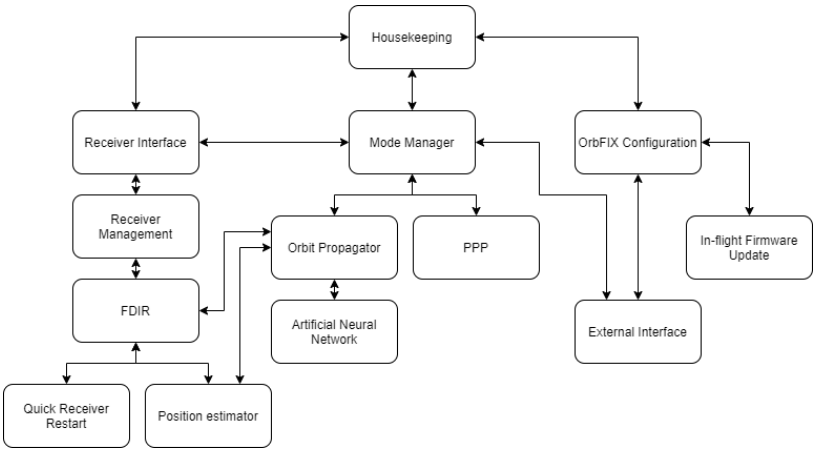

Figure 6.3: OrbFIX Software Architecture

the LEON3 based [30], Cobham GR716 controller. A real time operating system shall ensure timely execution of the implemented functions and facilitate the integration. Following a thorough investigation regarding availability, compatibility and support, the RTOS choice was made for OCEOS from OCE Technology. The OrbFIX controller interfaces both with the Mosaic receiver and an external "client", typically the satellite on-board computer. The Receiver Interface allows the receiver configuration through the Receiver Management. It is also the channel through which receiver measurements, either low level (pseudoranges) or high level (PVT), reach the Mode Manager. The Mode Manager switches between the three positioning modes (as per OFREQ-GEN-020):

- Low-power (orbit propagator and ANN)
- Nominal (GNSS + PPP corrections)
- Simple (standalone GNSS)

6.3 Orbit Propagator

The Orbit Propagator [24] has been developed and shall be integrated and tested on the Cobham GR716.

6.3.1 Design of the Orbit Propagator

Considering a positioning vector r, and a perturbing acceleration vector a_p, the equations of motion can be written in the form of:

$$\frac{d}{dt}\begin{bmatrix} r \\ \dot{\mathbf{r}} \end{bmatrix} = \begin{bmatrix} \dot{\mathbf{r}} \\ -\frac{\mu}{\|\mathbf{r}\|^3}\mathbf{r} + \mathbf{a_p} \end{bmatrix}$$

where μ is the gravitational parameter of Earth.

6.3.2 Mathematical model for perturbations

6.3.2.1 Third body

When a third body is considered, the resulting acceleration is described by:

$$\ddot{\mathbf{r}} = \mu_k \left(\frac{d_k}{\|d_k\|^3} - \frac{\rho_k}{\left\|\rho_k\right\|^3} \right)$$

in which d_k is the position vector from the k^{th} third body to the spacecraft and ρ_k is the position vector from the Earth to the k^{th} third body. The positions of the third bodies, i.e., Moon, Sun and Earth are provided by the JPL Developmental Ephemeris. The corresponding perturbing acceleration is

$$\mathbf{a_{3B}} = -\frac{G \cdot M_E}{{r_E}^3} - \frac{G \cdot M_S}{{r_S}^3} - \frac{G \cdot M_M}{{r_M}^3}$$

where

- G - newtonian constant of gravitation
- M_i - mass of the celestial body i (E - Earth, S - Sun, M - Moon)
- $\mathbf{r}_i$ - distance between the satellite and the celestial body i in ECI coordinates system

6.3.2.2 The J2 effect

The spin of the Earth leads to a redistribution of its mass which renders its shape an oblate spheroid; that makes the Earth slightly flatter around its poles and induces a gravitational perturbation which can be approximated by:

$$\ddot{\mathbf{r}} = -\frac{3}{2}\frac{J_2}{\|\mathbf{r}\|^4}\mu {R_E}^2 \left[\left(1 - 5\frac{{r_z}^2}{\|\mathbf{r}\|^2}\right)\frac{\mathbf{r}}{\|\mathbf{r}\|} + 2\frac{r_z}{\|\mathbf{r}\|}\begin{bmatrix} 0 \\ 0 \\ 1 \end{bmatrix} \right]$$

where R_E is the Earth's radius, r_z is the z component of the positioning vector $\mathbf{r} = (r_x, r_y, r_z)$, and J_2 is constant.

6.3.2.3 Solar radiation pressure

The solar radiation pressure is an external force acting on the satellite, created by sunlight hitting the body's surface. It is strongly dependent on the satellite's surface area and its reflectivity, and on the solar flux. The perturbing acceleration can be computed using:

$$\ddot{\mathbf{r}} = \mu \cdot p_s \cdot C_r \frac{A}{m} \left(\frac{1AU}{\|r_{Sat,S}\|} \right)^2 \frac{r_{Sat,S}}{\|r_{Sat,S}\|}$$

where μ is a shadow coefficient, p_s is constant, C_r is the reflectivity coefficient, A is the cross-sectional area of the satellite, m is the mass of the satellite and $r_{Sat,S}$ is the position vector from Sun's apparent position to the satellite.

6.3.2.4 Atmospheric drag

The equation of the acceleration induced by atmospheric resistance is:

$$\ddot{\mathbf{r}} = -0.5 \frac{A}{m} C_d \rho \|v\|^2 \frac{v}{\|v\|}$$

in which C_d is a drag coefficient, ρ is the atmospheric density and v is the velocity of the spacecraft relative to the atmosphere.

The results of the propagator performance evaluation are presented in fig. 6.4.

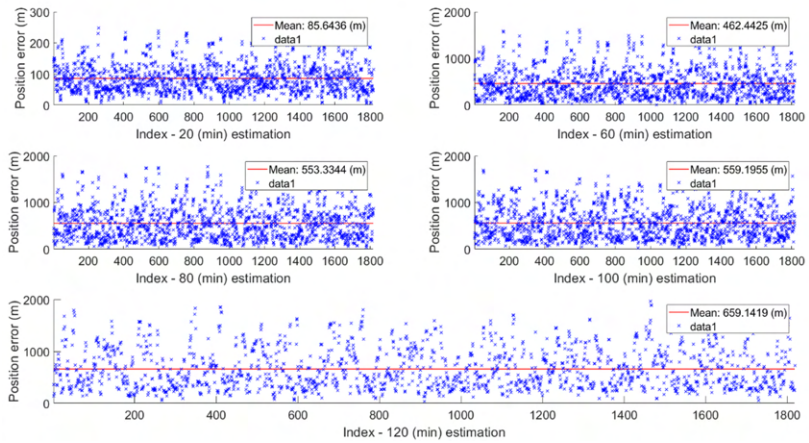

Figure 6.4: The position error (blue 'x') for 1800 random initial positions in July 2018 and 20, 60, 80, 100 and 120 minutes on-orbit trajectory estimation. The mean error is emphasized with the red horizontal line

6.4 Artificial Neural Network

Five artificial neural networks have been trained to improve the orbit propagator results [21]. The training data set consists of 10000 pairs of state vectors characterizing the beginning and ending points of 20, 60, 80, 100 and 120 minutes orbital segments chosen randomly over a one month period. The resulting neural networks have augmented the orbit propagator positions computed for the following month, and the relative errors are presented below [31].

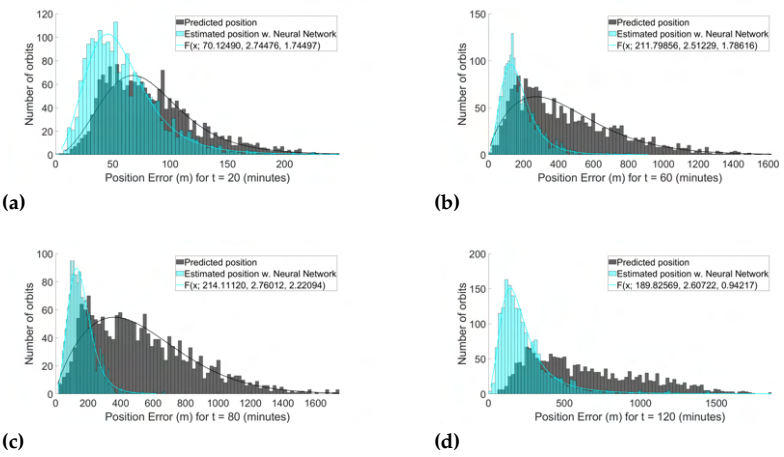

Figure 6.5: Positioning error distribution at (a)$t = 20$ minutes, (b)$t = 60$ minutes, (c)$t = 80$ minutes, (d)$t = 120$ minutes. The mean error for the predicted position (in gray) and the mean error for the estimated position (in cyan). The continuous cyan line represents the fitted Burr distribution.

It can be seen that the ANN improves significantly the output of the orbit propagator.

6.5 Fault Detection and Recovery

Reliability is an essential feature of space products. In order to maximize it, various techniques are employed, such as extensive testing, quality assurance for all components, redundancy, identification and removal of single points of failure. All these techniques imply additional costs and go against the "Components-Off-The-Shelf (COTS) philosophy" which aims at reducing costs even while assuming additional risks.

In order to increase reliability, two methods are envisioned: one making use only of the GNSS receiver data output and one comparing GNSS receiver output with orbit propagator output.

6.5.1 Fault detection with GNSS data only

Consider a discrete signal $x[n]$ with the sampling time $T_s = 1$ second. Moreover, let a single measurement be faulty at a time n_f, modeled using:

$$x[n_f] = (1 + \tau)x[n], \ \tau \in (0, 1) \, . \tag{6.1}$$

Let the size of the signal $x[n]$ be fixed, with the length $N = 10$. Then, compute the normalized auto-correlation of the signal x with:

$$R_x[m] = \begin{cases} \dfrac{1}{|R_x[0]|} \displaystyle\sum_{n=0}^{N-n-1} x[n+m]x^*[n], & m \geq 0 \\ R_x^*[-m], & m < 0 \end{cases} \tag{6.2}$$

Please note that, before using (6.2), compute $R_x[0]$ unnormalized.

Using the sequence R_x, compute:

$$\sigma = \text{diff}(\text{diff}(R_x)) \tag{6.3}$$

$$\text{diff}(x) = \{x(2) - x(1), x(3) - x(2), \ldots, x(n) - x(n-1)\} \tag{6.4}$$

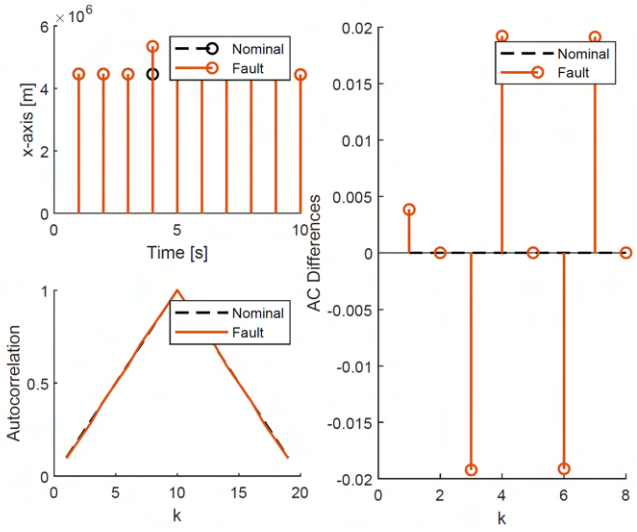

Figure 6.6: Example: fault at $n_f = 4$ seconds.

where σ is the approximate second-order derivative of the auto-correlation.

The presence of a fault in the signal $x[n]$ implies that σ has non-zero values in the interval $\overline{1, N} \setminus 5$.

Using σ, compute the following binary sequence:

$$b[n] = \begin{cases} 1, & \sigma[n] \neq 0\,, \\ 0, & \text{otherwise.} \end{cases} \tag{6.5}$$

n	1	2	3	4	5	6	7	8	$\sum$
$n_f = \{1, 10\}$	1	0	0	0	0	0	0	0	1
$n_f = \{2, 9\}$	1	1	0	0	0	0	0	1	1
$n_f = \{3, 8\}$	1	1	1	0	0	0	1	1	1
$n_f = \{4, 7\}$	1	0	1	1	0	1	1	0	1
$n_f = \{5, 6\}$	1	0	0	1	0	1	0	0	1

Table 6.1: Fault isolation using the binary sequence b.

The binary sequence b can uniquely isolate the time at which the error occurs. However, it is limited to the interval $\overline{1, 5}$ seconds, because of the auto-correlation's symmetry. The table shows the values of b for different fault times n_f.

Using the values from the columns $2, 3, 4$, the fault time n_f can be estimated such as:

- 1 or 10: $b_{2,3,4} = 0\,0\,0$
- 2 or 9: $b_{2,3,4} = 1\,0\,0$
- 3 or 8: $b_{2,3,4} = 1\,1\,0$
- 4 or 7: $b_{2,3,4} = 0\,1\,1$
- 5 or 6: $b_{2,3,4} = 0\,0\,1$

Once the first 10 samples are validated, it is easy to verify each new sample via a sliding window. In case of a fault, this shall be then isolated uniquely as the new sample.

6.5.2 Fault detection using GNSS data and orbit propagator predictions

Let $x(t)$ be the measured position on the x-axis from the GPS receiver. A useful approach to determine if a measurement at a given time t is faulty consists of comparing the measurement to another relevant value. Particularly, this approach uses predicted positions and compares the measurement to the corresponding predictions. Consider the predicted positions to be defined by $\widehat{x}(t)$. The prediction should be similar to the measured position, apart from unknown disturbances which cannot be accounted for when computing the prediction:

$$x(t) = \widehat{x}(t) + e(t)$$

Here, $e(t)$ signifies the unknown error between the measured and the predicted position. However, $e(t)$ is bounded by a maximum error ϵ_{max} which can be estimated apriori. Thus, any faulty measurement can be detected and located in time whenever:

$$e(t) = x(t) - \widehat{x}(t) > \epsilon_{max}$$

The concept is illustrated in Figure 6.8.

6.6 Electronic design

Considering the OrbFIX requirements, the design options and the components selection the OrbFIX electronic architecture is proposed in fig. 6.10. It includes the Cobham GR716 MCU and the Septentrio Mosaic-x5 GNSS receiver, an interface to the standard CubeSat PC104 BUS, an antenna connector and a current monitor. The GR716 requires also external RAM and FLASH memories.

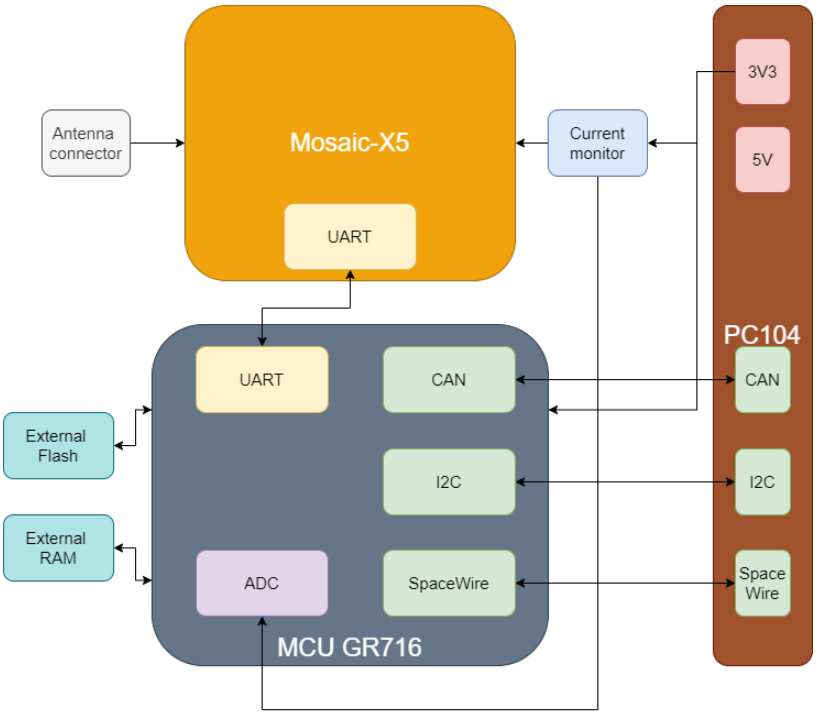

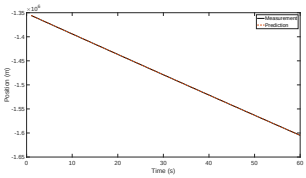

Figure 6.7: GRACE mission x-axis measured and predicted values

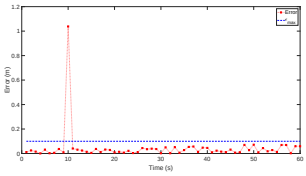

Figure 6.8: Fault detection using GRACE mission data. x-axis error between measured and predicted data. Faulty measurement is detected by comparison with the predefined ϵ_{max} threshold

Figure 6.9: Pumpkin CubesatKit protoboard (source: Pumpkin Inc.)

Figure 6.10: OrbFIX electronic architecture

Being a component dedicated to ground applications, Mosaic-X5 may be affected by single event effects (SEE) generated by high energy protons. This type of radiation shall be encountered in LEO orbits, as it was shown in 4.2. One way to detect and avoid receiver damage during such an event is to quickly cut power supply as soon as a sudden and unexpected raise of current is detected on the receiver power lines. Such a current surge may be caused by a SEE and could force a receiver reset, or, in the worst case, the destruction of the receiver. A simple current monitor shall be then implemented by measuring the voltage drop on a resistor place inline with the receiver supply. The measuring is done by the MCU via the analog-to-digital (ADC) block.

The OrbFIX electronic architecture is to be implemented on a 96 x 90 mm, CubeSat standard printed circuit board (PCB). Such a board includes two PC104 connectors that shall form the satellite BUS. An example of a CubeSat prototyping board from Pumpkin Inc. is shown in fig. 6.9. The two PC104 connectors shall be used by OrbFIX to interface with the on-board computer via one (or several) of the included interfaces: CAN, I2C and SpaceWire. It shall be also used to power the receiver and the MCU.

7 Testing

This chapter shall define a set of tests that need to be passed in order to fulfill the OrbFIX requirements. It shall then present the results of these tests as they were ran upon the COTS GNSS receiver.

7.1 Physical testing

7.1.1 Thermal-vacuum test

For the first iteration of the test, one of the two functional receivers that were irradiated was used. The test started with a cold temperature portion without identifying any issues. On the hot segment of the test, the device became un-operational when the temperature exceeded +55 °C. After the hot storage portion of the test it was confirmed, that under the threshold temperature the device was operating nominally. It was assumed, and later confirmed, that the behaviour is caused by the high temperature stress adding to the defects induced by the radiation.

A second iteration of the TVAC test was performed with a new, un-irradiated Mosaic receiver. It was considered that only the operational range of temperatures needs to be confirmed. This final test consisted of two segments: one for high temperature and one for the low temperature. The TVAC test setup is presented in fig. 7.1.

The internal temperature sensor of the Mosaic receiver reaches up to 78 °C, with no visible degradation of the functionality. No drop in the number of tracked and PVT-used satellites can be traced to another reason than the receiver antenna – satellite geometry. The same can be said also for the PVT error (fig. 7.3) and C/N0 measurements. It can be noted that the antenna placement was far from ideal, being close to a wall and having a clear horizon only towards South.

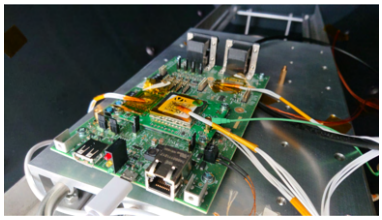

Figure 7.1: TVAC setup for the Septentrio Mosaic test

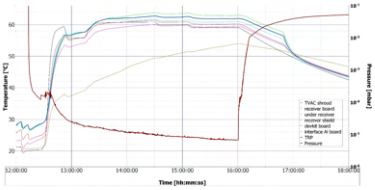

Figure 7.2: Temperature and pressure evolution during the Mosaic receiver high temperature TVAC test

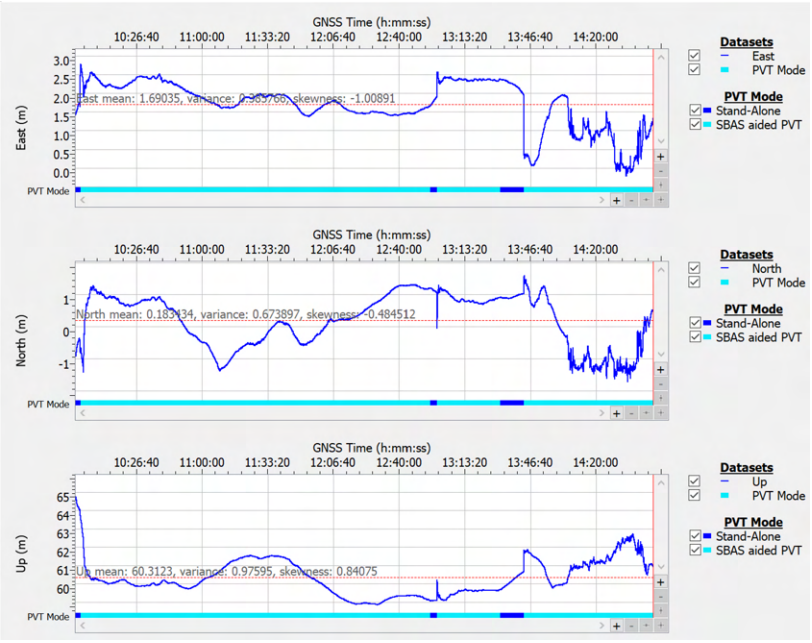

Figure 7.3: PVT error evolution during the Mosaic receiver high temperature TVAC test

Figure 7.4 presents the overview of temperature and pressure evolution during the low temperature TVAC test. In order to get the TRP below -30 °C during receiver operation, the TVAC shroud was set initially to -40 °C, then to -55 °C and finally to -50 °C. The TRP crossed -30 °C after about 140 minutes and was maintained below this value for almost three hours. During this time the pressure was maintained in the order of 10^{-6} mbar.

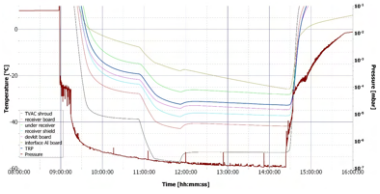

Figure 7.4: Temperature and pressure evolution during the Mosaic receiver low temperature TVAC test

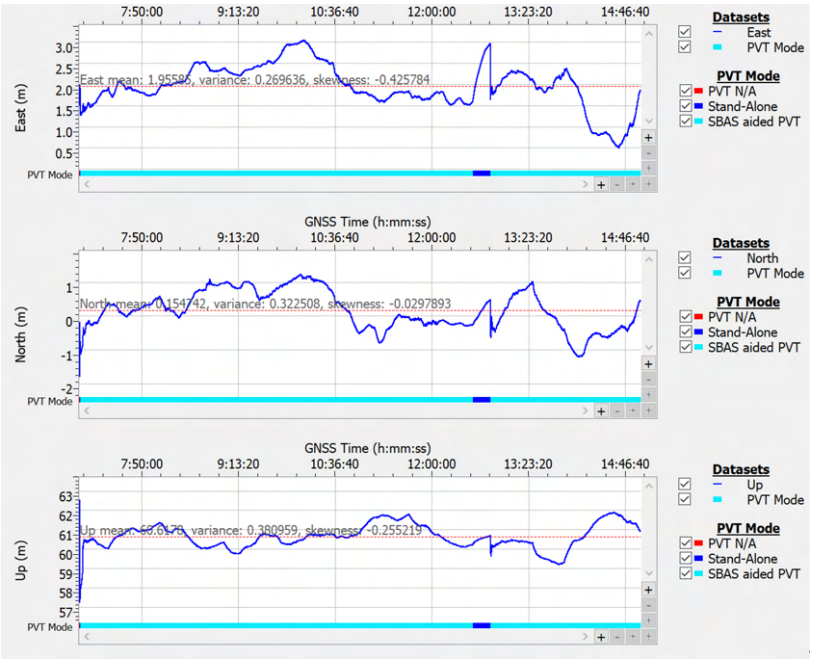

Figure 7.5: PVT error evolution during the Mosaic receiver low temperature TVAC test

7.1.2 Balloon testing

The testing campaign of the Mosaic COTS receiver included an in-flight verification on a high-altitude balloon. One of the reasons for the test

was to evaluate performance of a commercial receiver under conditions exceeding the COCOM altitude limits. As such, the Mosaic version integrated a COCOM restricted receiver, which behaves normally when the altitude limit was exceeded. Two balloon tests were performed, as the first one failed to reach the target altitude of above 30000 m.

The first test reached 14000 m when, due to strong winds, the payload detached from the balloon and fell.

A picture of the balloon test setup is presented in 7.6

During the flight, the payload section separated from the balloon and the parachute before reaching the maximum altitude, resulting in a rapid fall. The initial fall rate is higher than 30 m/s and the final vertical velocity at impact was higher than 20 m/s. The payload was recovered after the flight.

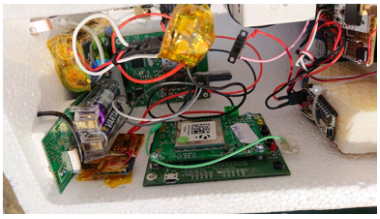

Figure 7.6: Balloon test setup

Figure 7.7: Ascension and fall of the balloon box as recorded by the Mosaic receiver

It can be seen in 7.7 that the profile of the ascension is accurately monitored by the Mosaic receiver. After the start of the fall the receiver seems to be turned off for more than 270 s, after which it immediately recovers PVT. In the first part of the climb, the internal temperature reaches 70 °C (7.8), due to the well-insulated box in which is located along with other electronics. However, the temperature drops with the height, just prior to the fall start reaching 38 °C. The continuous drop of temperature seems in line with the hypothesis that during the first part of the fall the receiver was off.

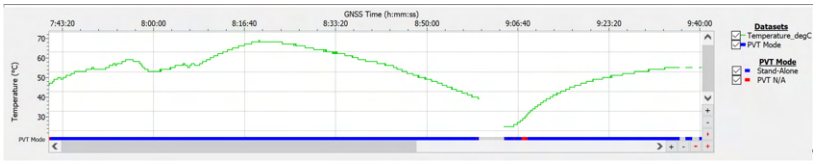

Figure 7.8: Temperature profile indicated by the internal sensor of the Mosaic receiver

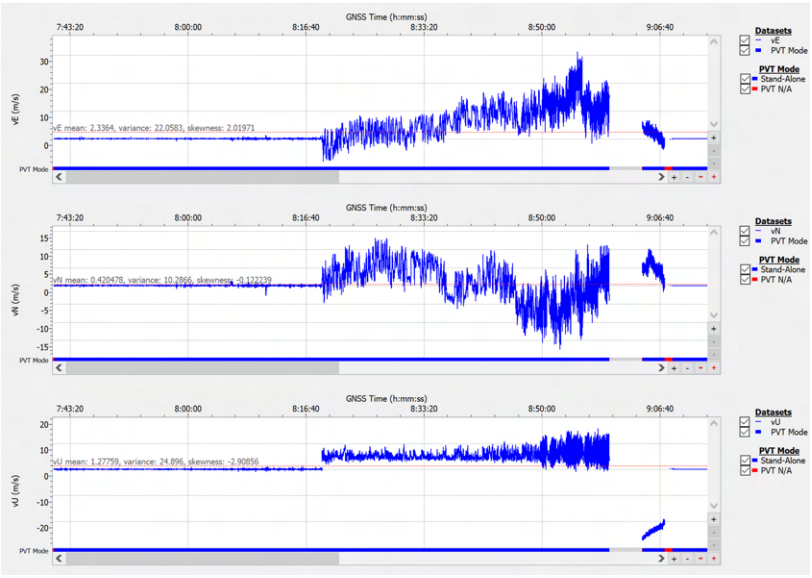

Figure 7.9: Velocity components for the first balloon test of the Mosaic receiver

The second balloon test reached almost 36000 m. However, as the receiver used in the first test was lost, one that has been used in the irradiation campaign was used. Figure 7.11 presents the altitude profile of the second balloon flight. A data gap can be observed during a 15 minutes period.

Figure 7.10: Google Earth view of the balloon track

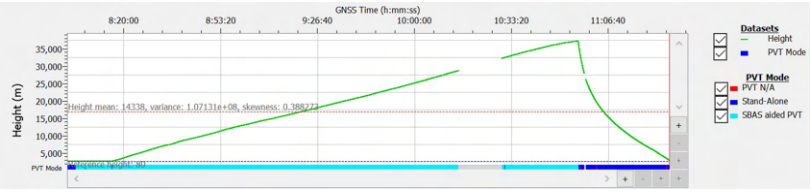

Figure 7.11: Ascension and descent of the second balloon payload as recorded by the Mosaic receiver

Figure 7.12: Temperature profile indicated by the internal sensor of the Mosaic receiver

Both balloon tests proved the reliability and robustness of the Mosaic receiver contributing to building trust in the proposed COTS solution.

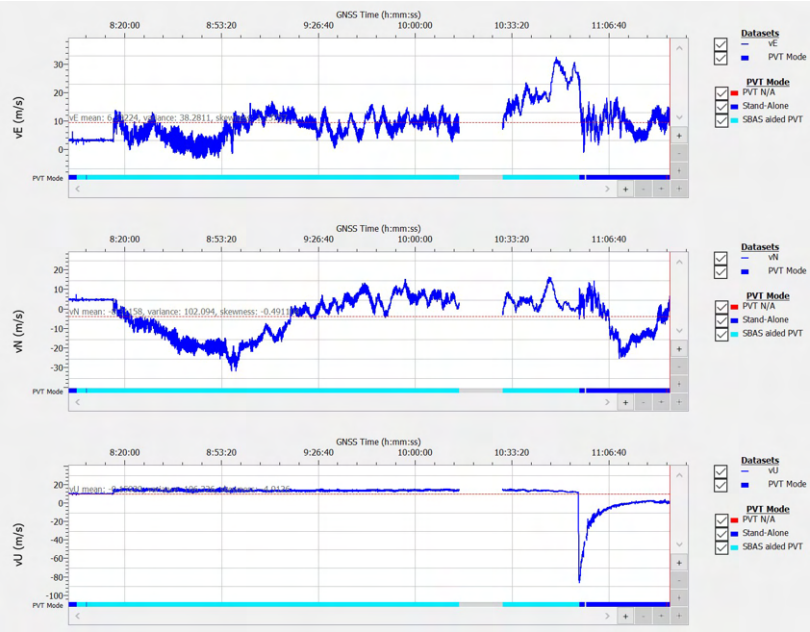

Figure 7.13: Velocity components for the balloon test of the Mosaic receiver

7.2 Functional testing

A Spirent GSS7700 simulator, available in the European Navigation Laboratory of the European Space Agency, has been used to simulate the low Earth orbit presented in fig. **??**. The simulated orbit has been recorded for future replays in order to allow fine-tuning of the receiver in the lab.

The functional test was successful, with slightly better results obtained with L5/E5 (positioning errors lower than 2 m), compared to L1/E1 (positioning errors above 2 m on two of the axis). In fig. 7.14c, both GPS and Galileo constellations and L1/E1 and L5/E5 frequencies have been used simultaneously over more than two orbits (approx. 5400 s/orbit). The average error on each axis was 1.35 m on x, 0.47 m on y and 0.78 m on z. The average 3D error was 1.64 m. These results are very encouraging as no corrections have been applied.

The receiver performed constant tracking of satellites and did not present any issues with the high velocity, Doppler shifts and Doppler rates.

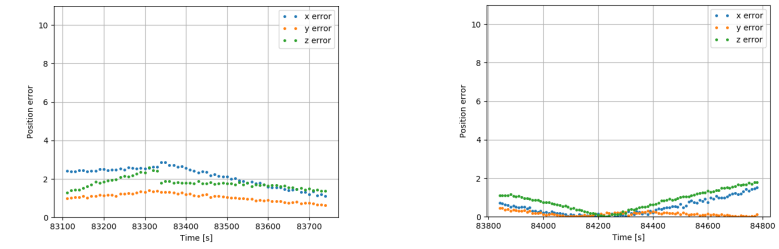

(a) (b)

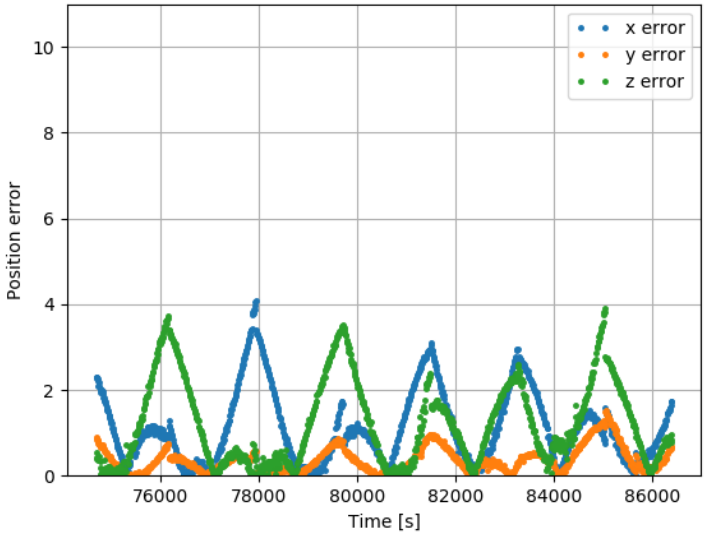

(c)

Figure 7.14: Positioning errors in meters relative to the simulated orbit: (a) Multi-constellation (GPS, Galileo), single frequency (L1/E1); (b) Multi-constellation (GPS, Galileo), single frequency (L5/E5); (c) Multi-constellation (GPS, Galileo), multi-frequency (L1/E1, L5/E5);

7.3 Total Irradiation Dose (TID) test

As discussed in the test plan, the TID test of the Mosaic receiver is essential for assessing its suitability for space use. Such a test has been performed using the Gamma Chamber 5000 Co-60 irradiation source of the IFIN-HH.

7.3.1 Test setup

In order to increase the test relevance, three Septentrio Mosaic-X5 receivers have been tested. The three receivers have been powered during the irradiation and current consumption has been monitored using INA219, an integrated circuit current monitor from Texas Instruments. OpenLog, an Arduino based logging device, has been used to log the current used by the receivers.

The three receivers are stacked and the three antenna connectors are attached together to a plastic support. One OpenLog and three INA219 are seen stacked at the left. Two dosimeters have been included, one on top and another one in the middle of the receiver stack.

Figure 7.15: OpenLog

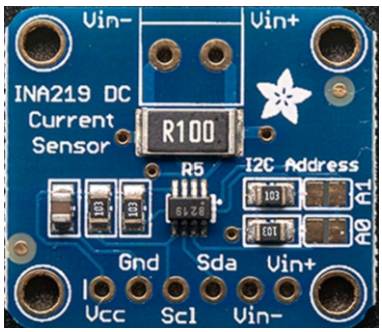

Figure 7.16: TI INA219 current monitor

	After 1st irrad.	After 2nd irrad.	After 3rd irrad.
Target dose [krad]	3.3	10	30
Dosimeter [krad]	3.55	10.65	35.58

Table 7.1: Total doses measured after each irradiation session

	Average SV		TTF (s)	Temp (°C)	C/N0 G04 elev. 75°	C/N0 E04 elev. 75 °
	Track	PVT				
Witness	35	20	30	45	47 dB-Hz	42 dB-Hz
RAD1	-	-	-	-	-	-
RAD2	31	20	50	50	49 dB-Hz	42 dB-Hz
RAD3	-	-	-	-	-	-

Table 7.2: Key functionality parameters recorded after the third session of irradiation

7.3.2 Test description and results

The receivers have been placed in the middle of the Gamma Chamber 5000 sample chamber, as seen in fig. 7.18.

Considering the 0.27 Mrad/h gamma flux, the first dose of 3.3 krad was obtained after 47 seconds. The receivers were powered during the test, using the same power supply placed outside the radiation chamber. The average total consumption was 1.05 A at 6.82 V.

Based on the requested irradiation dose, the duration for the three exposure intervals was computed with respect to the characteristics of the installation. Considering the 76 rad/s gamma flux, the first dose of 3.3 krad was obtained after 47 seconds. The subsequent sessions were 94 and 330 seconds. Two dosimeters were used to measure the actual dose of irradiation received by the DUT. As expected, there was a slight difference in the total dose measured by the two dosimeters: 35.02 and 36.14 krad respectively. The dosimeter placed in the middle of the stack show the lower value, but the difference is only 3.2% (table 7.1).

7.3.2.1 Third irradiation session

First two irradiation sessions were performed with no noticeable effects on the receivers except a slight increase in temperature. After exchanging the SD card with new ones, a third radiation session was started. In this one, a total of 30 krad, three times the expected life-time dose was to be reached after 330 s. However, after 300 s, the current draw started to drop, as shown in 7.19. Ending the exposure, none of the Mosaic LEDs were functioning. A functional test was performed. None of the SD cards was readable, indicating their total failure. Out of the three tested receivers, two of them, RAD1 and RAD2 were detected and connected to the computer, but only RAD2 was able to acquire signals and obtain a PVT solution. For this one, the only parameter changing compared to the previous functioning tests was its temperature, which grew more than 5 degrees to 50 °C. 24 hours later, the RAD1 receiver recovered full functionality, while RAD3 was able to connect to the computer acquire signals but behave erratically and not being able to compute PVT.

The readings from the dosimeters indicated that the estimated total exposure doses were slightly higher than the estimated values before the test of 35 krad and 36 krad respectively. The table 7.1 shows the expected and the actual doses. The TID test was passed successfully by the Mosaic

Figure 7.17: Functional testing antenna setup

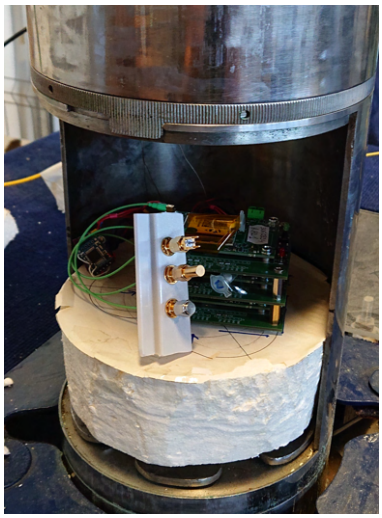

Figure 7.18: Sample chamber position of the test setup

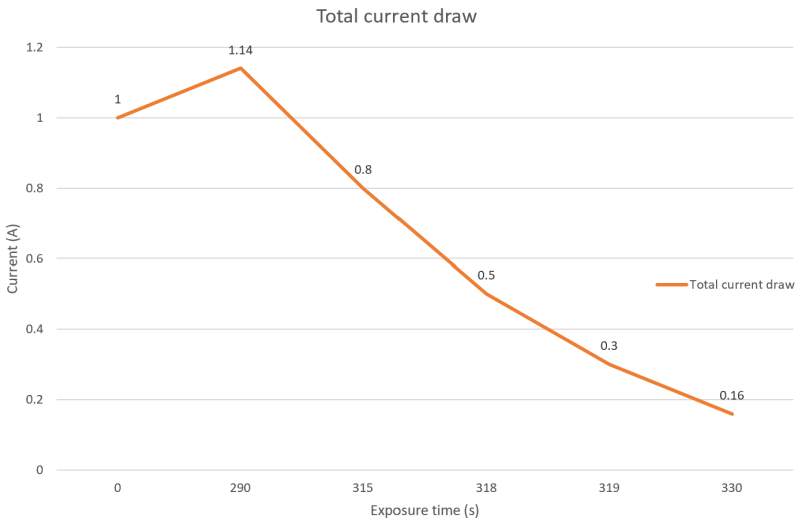

Figure 7.19: Current drop during third radiation exposure

receivers, indicating that they may be used for space applications with no additional shielding.

7.4 Testing conclusions

Before integrating a satellite subsystem, trust needs to be built regarding the robustness of the components and their capacity to properly fulfil their roles in order to attain the subsystem requirements. For space-grade components, this trust is built upon the manufacturer specifications and the flight heritage. For Components-Off-The-Shelf, the manufacturer specifications are not covering space usage and, most of the times, there is no flight heritage. In the case of OrbFIX, part of the components, the ones overseeing the operation of the subsystem and providing the interface withe the satellite BUS, are radiation hardened space grade components with extended flight heritage. However, the critical component, the GNSS receiver, is COTS with no flight heritage. Several tests were designed and performed in order to ensure its robustness and performance. The Septentrio Mosaic COTS GNSS receiver has been tested in environments simulating a low Earth orbit from the point of view of temperature, pressure, radiation and GNSS signals. It has been also tested in a high altitude balloon, which concluded in a high velocity impact test. The receiver passed all tests and its integration in the OrbFIX PPP GNSS receiver for space can continue.

Conclusions 8

In the previous chapters the initial development stages of a Precise Point Positioning Global Navigation Satellite System receiver for space was described from motivation and theoretical background to design approach, requirements identification, preliminary design and preliminary components testing. The originality of this thesis consists in the approach to the problem, in the fact that more than being just a GNSS receiver, OrbFIX is a flexible positioning system, in the implementation of Artificial Neural Networks for improving the positioning with little energy expenditure and in the thorough testing procedure insuring a high level of robustness for components.

The approach regarding the development of a PPP GNSS receiver for space employed for OrbFIX is original in two ways. First, in order to minimize the costs of the development and of the final product a regular GNSS receiver chipset has been used. This solution is part of a wider movement in the space industry which aims at integrating Components-Off-The-Shelf (COTS) instead of specialized space products. This is done in order to reduce the costs of space missions and take advantage of latest technologies before they make their tedious way into traditional, space-grade products. Besides the original idea, personal contributions were in the comparison and selection of the OrbFIX components. The Septentrio Mosaic receiver was selected due to its small size, small power consumption and range of capabilities, including its extensive list of configurable parameters. These aspects have been presented in the article:

- Alexandru Pandele et al. 'COTS based GNSS Receiver with Precise Point Positioning for CubeSats'. In:MATEC Web of Conferences 304 (2019). [1]
- Alexandru Pandele et al. 'OrbFIX - Precise Positioning and Machine Learning on a Cubesat GNSS Receiver', accepted abstract in 72nd International Astronautical Congress, Dubai 2021

While being cheaper and more effective, COTS are often less reliable and even more so in the punishing space environment. The OrbFIX original approach is to combine COTS with space-grade components that can identify and recover COTS faults. This is done by using the highly reliable GR716 Leon 3 micro-controller which allows the implementation of a Fault Detection, Identification and Recovery algorithm.

The OrbFIX requirements definition in chapter 5, is a personal contribution underlined by the co-autorship of the following articles describing various space missions:

- Alexandru Pandele et al. 'Cube-sat Formation Flying: A Suitable Platform For Space Situational Awareness'. In:61st InternationalAstronautical Congress(2010) [32]
- Alexandru Pandele et al. 'Pluribus -Nanosatellites Formation'. In:60th International Astronautical Congress(2009) [33]

- Alexandru Pandele et al. 'Scientific Experiments On Board The Goliat Cubesat'. In:62nd International Astronautical Congress, Cape Town,South Africa(2011) [34]
- Alexandru Pandele et al. 'Past,Present And Future Of The Romanian Nanosatellites Program'. In:62nd International Astronautical-Congress(2011) [35]
- Alexandru Pandele et al. 'Autonomous close-proximity operations in space: The PRoBa-3 rendezvous experiment (P3RVX)'. In:69th InternationalAstronautical Congress (IAC 2018)(2018) [25]

The requirements definition implied trading off space environment and small satellite mission constraints with necessary performance and features and focused on CubeSat missions in Low-Earth-Orbit, but not exclusively. This gives limits on the size and mass of the OrbFIX subsystem, as well as on the available power. The choice of orbit is providing an estimation on the radiation exposure during a one-year mission. Regarding performance and features, two main objectives led the requirements definition: high availability and precise positioning. These two objectives were translated in the employment of several high-reliability components, the necessity of a FDIR algorithm and the integration of various GNSS augmentation methods, including Precise Point Positioning with ground station corrections, Galileo High Accuracy Service (HAS) and Space Based Augmentation Systems (SBAS).

Thus, OrbFIX is original by being a flexible positioning system that may be used in several modes, based on the amount of information and on the amount of power available. It may operate simply in a low power mode, providing an estimated position via a light orbit propagator. When a sufficient amount of data has been collected from the GNSS receiver, an Artificial Neural Network may be trained and used to augment the quality of the orbit propagator's estimations. The usage of a COTS, ground based receiver makes it possible to access the latest Galileo corrections, the High Accuracy Service, that are broadcast on Galileo frequency E6 and that allow precise point positioning errors of less than 20 cm. Last, but not least, OrbFIX may receive PPP corrections directly from a Ground Station, using the satellite communication system and provide positions with an accuracy of less than 10 cm.

The preliminary design of the OrbFIX susbsystem is continued in chapters 6 and 7 by showing whether and how the requirements in chapter 5 are feasible. Two design choices are examined, which trade off between the GNSS correction source and the complexity and power consumption of the OrbFIX subsystem. The simpler and low power design is chosen, having the advantage of allowing a future upgrade that implements missing functionalities at the expense of increased complexity and power usage.

The software architecture has been designed around the three operation modes. It integrates communication interfaces with the satellite BUS and the on-board computer, as well as with the GNSS receiver. Besides the software architecture itself, the mode manager, the integration of the orbit propagator, the integration of the artificial neural network and the FDIR modules represent original contribution.

A light version of an orbit propagator algorithm was implemented. This is necessary in order to reduce the computation time and power con-

sumption. The orbit propagator was initially implemented in MATLAB and then ported in C for implementation in the GR716 microcontroller. Personal contributions on the orbital propagator are included in the following papers:

- Alexandru Pandele et al., 'Trajectory analysis for Cubesat landing on Didymoon in context ofAIM mission'. In:68th International Astronautical Congress, Adelaide, Australia(2011) [24]
- Alexandru Pandele et al. 'Autonomous close-proximity operations in space: The PRoBa-3 rendezvous experiment (P3RVX)'. In:69th InternationalAstronautical Congress (IAC 2018)(2018) [25]

The FDIR is able to detect positioning errors and the thesis shows how this can be done by comparing the PVT solution to the output of an orbit propagator, or, independently, by detecting jumps in a series of positioning solutions. The FDIR was designed to detect errors triggered by high-energy nucleon particles radiation (Single Events Errors - SEE), by continuous monitoring of the receiver current draw. In case of a SEE, an unjustified increase in the current draw is observed and the micro-controller powers down the receiver. This is part of the Recovery algorithm that aims at maximizing OrbFIX availability by minimizing the time it is unable to provide a positioning solution. Moreover, an algorithm was developed that shall provide accurate estimated positions during the receiver restart. The algorithm is based on an orbit propagator that is initialized by the latest valid position and can provide accurate positioning with errors lower than 10 cm for the first minute of propagation (see fig. 6.8).

The Artificial Neural Network (ANN) was developed as a nonlinear estimator improving the position estimate of the Orbit Propagator. The ANN implies a training period and an effectiveness period. During the training period, usually a month, precise orbital positions are recorded by the GNSS receiver and fed to the ANN. Following that, the effectiveness period allows the ANN to improve the position estimate of the Orbit Propagator by up to 70% after 80 minutes (fig. 6.5c).The effectiveness period lasts about a month, after which the ANN improvement diminishes. The development of the ANN is also described in the following articles:

- Alexandru Pandele et al. 'Multipath Prediction Model for Global Positioning Satellites Using NeuralNetwork'. In:68th International Astronautical Congress, Adelaide, Australia(2011) [27]
- Alexandru Pandele et al. 'Improving Satellite On-Board Orbit Estimation with Artificial Neural Networks'.In:presented at 71st International Astronautical Congress the Cyberspace Edition(2020) [21]
- Alexandru Pandele et al. 'ImprovingGNSS Positioning of Satellites using Artificial Neural Networks'. In:MATEC Web of Conferences 304 (2019) [31]

To compensate for the COTS usage, a comprehensive test procedure has been devised based on available standards defined by the European Space Agency. Radiation, thermal-vacuum and balloon tests have been performed in order to ensure the robustness of the COTS components, as well as functional tests simulating orbital operation. Personal contributions were in:

- definition of test procedures
- execution of test procedures
- assessment of test results

A comprehensive radiation test was performed at the Horia Hulubei National Institute for Physics and Nuclear Engineering. The test focused on assessing the impact of the radiation dose accumulated over the mission duration on a low Earth orbit. The test proved that the most critical OrbFIX component, the GNSS COTS receiver shall survive the mission and, with some additional shielding, may survive three times the mission duration. The test consisted in the irradiation of three sample GNSS receivers in three stages. After each irradiation stage, the receivers were tested and their basic performance analysed. The radiation test and follow up thermal-vacuum tests pointed to two different failure modes caused by extended radiation exposure. In one failure mode, the receiver capability of powering the antenna was lost, indicating a failure of the antenna power supply. The other failure mode consisted of a sensitivity to the thermal environment. After irradiation, one of the receivers powered down when the temperature reached +55 °C. These two failure modes indicate how to improve the robustness of the COTS receivers for their usage in space missions.

A thermal-vacuum test has been performed for testing the COTS GNSS receivers for the entire range of temperatures expected to be encountered on a low Earth orbit. The test was performed at a similar vacuum level as the one expected in space. The receiver operated nominally, with no drop of performance on the entire operational temperature range, proving that COTS components could withstand space environment.

Two balloon tests were performed, aiming at testing the COTS GNSS receivers in an environment outside the laboratory and as close as possible to the one encountered in a space mission. The balloons brought the receivers first up to 14000 m and then to more than 34000 m. In both cases the behaviour of the receivers was as expected, considering that for the second balloon test an irradiated receiver was used. The receivers responded well in conditions of strong, random movements caused by the winds, being able to track the accurate position of the balloon payload during all flight. Following the first flight, the receiver tracked and survived an unscheduled fall and impact with 21 m/s. During the second flight, the irradiated receiver powered down during a 15 min interval when its temperature was in the range of +50 °- +55 °C. Besides this gap, it was able to track the rest of the flight, including the initial drop of 96 m/s following the balloon explosion.

While the balloon tests provided a insight regarding the operation of the receiver in an operational environment, they were not able to come close to simulating the signal dynamics expected on orbit. For this, a GNSS signal simulator was used. With no augmentation, the receiver provided positioning with 3D errors lower than 1.7 m when using dual frequency GPS and Galileo constellations, proving that the COTS receiver is able to cope with the high Doppler shifts and Doppler shift rates that are experienced on a low Earth orbit, despite being designed for ground applications.

The purpose of the thesis was to advance the development of a Precise Point Positioning Global Navigation Satellite Systems receiver for space,

from idea up to a preliminary design. These development phases include: the review of the theory governing precise positioning and navigation; the consolidation of the requirements for a PPP GNSS receiver for space; identification, development and testing of key features (ANN augmented orbit propagator, FDIR); identification and testing of critical components; and preliminary hardware design. Following the preliminary design, further development is necessary, up to critical design, testing, qualification and in-orbit demonstration. However, at this stage the feasibility of the project is proven and the trust in a final product that is both robust and accurate is built.

This being said, while based on a personal idea and embedding original contributions both in terms of concept and implementation, the development of such a complex object as the OrbFIX space receiver could not have been done without the support of the Romanian InSpace Engineering team that I led (Ștefan Mihai, Costi Cherciu, Antonia Croitoru, Claudiu Cherciu, Rareș Apostol, Dan Șelaru, Marius Trușculescu, Claudiu Drăgășanu and Mugurel Bălan) and the financing of the European Space Agency through the General Support Technology Programme.

Bibliography

Here are the references in citation order.

[1] **Alexandru Pandele**, Costel Cherciu, Marius Trușculescu, Claudiu Drăgășanu, and Sergiu-Ştefan Mihai. 'COTS based GNSS Receiver with Precise Point Positioning for CubeSats'. In: *MATEC Web of Conferences* 304 (2019). DOI: 10.1051/matecconf/201930407009 (cited on pages 1, 35).

[2] Angus Stevenson. *Oxford dictionary of English*. Oxford University Press, USA, 2010 (cited on page 2).

[3] Eva Germaine Rimington Taylor, K St B Collins, and Joseph Needham. *The haven-finding art: a history of navigation from Odysseus to Captain Cook*. Hollis & Carter London, 1971 (cited on page 2).

[4] Julian A Smith. 'Precursors to Peregrinus: The early history of magnetism and the mariner's compass in Europe'. In: *Journal of Medieval History* 18.1 (1992), pp. 21–74 (cited on page 2).

[5] Samuel L Macey. *Time: A bibliographic guide*. Routledge, 2018 (cited on page 2).

[6] WF Blanchard. 'Air Navigation Systems Chapter 4. Hyperbolic Airborne Radio Navigation Aids–A Navigator's View of their History and Development'. In: *The Journal of Navigation* 44.3 (1991), pp. 285–315 (cited on page 2).

[7] Catherine Alexander. 'The Story of GPS'. In: *50 Years of Bridging the Gap*. Ed. by DARPA. 2008 (cited on page 2).

[8] Harold D Black. 'Early development of transit, the navy navigation satellite system'. In: *Journal of Guidance, Control, and Dynamics* 13.4 (1990), pp. 577–585 (cited on page 2).

[9] Bradford W Parkinson and Stephen W Gilbert. 'NAVSTAR: Global positioning system—Ten years later'. In: *Proceedings of the IEEE* 71.10 (1983), pp. 1177–1186 (cited on page 2).

[10] GM Polischuk, VI Kozlov, VV Ilitchov, AG Kozlov, VA Bartenev, VE Kossenko, NA Anphimov, SG Revnivykh, SB Pisarev, AE Tyulyakov, et al. 'The global navigation satellite system GLONASS: Development and usage in the 21st century'. In: *Proceedings of the 34th Annual Precise Time and Time Interval Systems and Applications Meeting*. 2002, pp. 151–160 (cited on page 3).

[11] **Alexandru Pandele**, Antonia Croitoru, Andrei Hulea, Costel Cherciu, Alina Răduțu, Marco Porretta, Peter Buist, Dumitru Andrescu, Lucian Duțu, Claudiu Drăgășanu, Marius Trușculescu, and Mugurel Bălan. 'GALILEO and GPS Performance in the Maritime Environment'. In: *presented in 33th International Technical Meeting of The Satellite Division of the Institute of Navigation (Virtual ION GNSS+ 2020)* (2020) (cited on page 3).

[12] Li Chengzhi. 'The Chinese GNSS—System development and policy analysis'. In: *Space Policy* 29.1 (2013), pp. 9–19 (cited on page 3).

[13] Atsushi Shimamura. 'MSAS (MTSAT satellite-based augmentation system) project status'. In: *Air & Space Europe* 1.2 (1999), pp. 63–67 (cited on page 3).

[14] Kanta Prasad Sharma and Ramesh C Poonia. 'Review study of navigation systems for indian regional navigation satellite system (IRNSS)'. In: *Soft Computing: Theories and Applications*. Springer, 2018, pp. 735–742 (cited on page 3).

[15] GPS-SPS. *GPS Standard Positioning System Performance Standard*. Sept. 2008 (cited on page 4).

[16] Yuanxi Yang, Weiguang Gao, Shuren Guo, Yue Mao, and Yufei Yang. 'Introduction to BeiDou-3 navigation satellite system'. In: *NAVIGATION, Journal of the Institute of Navigation* 66.1 (2019), pp. 7–18 (cited on page 4).

[17] Peter J.G. Teunissen and Olviver Montenbruck. *Springer Handbook of Global Navigation Satellite Systems*. Springer, 2017 (cited on pages 5, 7).

[18] J.S. Subirana, J.M.J. Zornoza, and M. Hernandez-Pajares. *GNSS Data Processing*. ESA Communications, May 2013 (cited on pages 6, 7).

[19] Viet Duong, Ken Harima, Suelynn Choy, and Chris Rizos. 'Multi-frequency multi-GNSS PPP: a comparison of two ambiguity resolution methods'. In: *Proceedings of the International Global Navigation Satellite Systems Association IGNSS Symposium*. 2020, 5e7 (cited on page 11).

[20] Sven Müncheberg, Manfred Krischke, and Norbert Lemke. 'Nanosatellites and micro systems technology—capabilities, limitations and applications'. In: *Acta Astronautica* 39.9-12 (1996), pp. 799–808 (cited on page 14).

[21] **Alexandru Pandele**, Sergiu-Ştefan Mihai, Dan Șelaru, Mihnea Ion, and Mugurel Bălan. 'Improving GNSS Positioning of Satellites using Artificial Neural Networks'. In: *MATEC Web of Conferences* 304 (2019). DOI: 10.1051/matecconf/201930407010 (cited on pages 14, 22, 37).

[22] Edward Petersen. *Single event effects in aerospace*. John Wiley & Sons, 2011 (cited on page 14).

[23] ESA Radiation. *Radiation Design Handbook*. Tech. rep. ESA PSS-01–609 Issue 1, 1993 (cited on page 15).

[24] **Alexandru Pandele**, Mugurel Bălan, Dan Șelaru, Mihai Racheru, Claudiu Drăgășanu, Marius Trușculescu, Silvana Radu, and David Binns. 'Trajectory analysis for Cubesat landing on Didymoon in context of AIM mission'. In: *68th International Astronautical Congress, Adelaide, Australia* (2011) (cited on pages 15, 20, 37).

[25] Paulo Rosa, Pedro Freire Silva, Baltazar Parreira, Miguel Hagenfeldt, Andrea Fabrizi, Antonio Pagano, Antonio Russo, Samuele Salvi, Murray Kerr, Silvana Radu, Anthonius Daoud-Moraru, **Alexandru Pandele**, Adrian Mihail Stoica, Sergiu Stefan Mihai, David A. K. Pedersen, John Leif Jørgensen, Sergio Tiraplegui Riveras, Rafael Contreras, Alexander Cropp, and Jonathan Grzymisch. 'Autonomous close-proximity operations in space: The PRoBa-3 rendezvous experiment (P3RVX)'. In: *69th International Astronautical Congress (IAC 2018)* (2018) (cited on pages 15, 36, 37).

[26] Paulo Rosa, Baltazar Parreira, Andrea Fabrizi, Antonio Pagano, Samuele Salvi, I. Grozea, Murray Kerr, **Alexandru Pandele**, Sergiu Stefan Mihai, Dan Șelaru, Rareș Apostol, Lăpușneanu Alexandru, Mihai Racheru, Sergio Tiraplegui Riveras, Rafael Contreras, and Jonathan Grzymisch. 'A Functional Engineering Simulator for Close-Proximity Operations: The Proba-3 RendezVous eXperiment (P3RVX) FES'. In: *7th International Workshop on Numerical Modelling in Aerospace Sciences, "NMAS 2019", Bucharest, Romania* (2019) (cited on page 15).

[27] Silvana Radu, **Alexandru Pandele**, Mihnea Ion, Antonia Croitoru, Marius Trușculescu, Claudiu Drăgășanu, and Dan Șelaru. 'Multipath Prediction Model for Global Positioning Satellites Using Neural Network'. In: *68th International Astronautical Congress, Adelaide, Australia* (2011) (cited on pages 15, 37).

[28] J.F. Zumberge, M.B. Hein, D.C. Jefferson, M.M. Watkins, and F.H. Webb. 'Precise Point Positioning for the efficient and robust analysis of GPS data from large networks'. In: *Journal of Geophysical Research: Solid Earth 102(B3)* (1997) (cited on page 15).

[29] Cal Poly SLO The CubeSat Program. *CubeSat Design Specification Rev 13*. Feb. 2014 (cited on page 17).

[30] Jiri Gaisler. 'A portable and fault-tolerant microprocessor based on the SPARC v8 architecture'. In: *Proceedings International Conference on Dependable Systems and Networks*. IEEE. 2002, pp. 409–415 (cited on page 20).

[31] **Alexandru Pandele**, Sergiu-Ştefan Mihai, Dan Șelaru, Marius Trușculescu, Mugurel Bălan, and Claudiu Drăgășanu. 'Improving Satellite On-Board Orbit Estimation with Artificial Neural Networks'. In: *presented at 71st International Astronautical Congress the Cyberspace Edition* (2020) (cited on pages 22, 37).

[32] **Alexandru Pandele**, Mugurel Bălan, M. Piso, Marius Trușculescu, and Claudiu Drăgășanu. 'Cubesat Formation Flying: A Suitable Platform For Space Situational Awareness'. In: *61st International Astronautical Congress* (2010) (cited on page 35).

[33] **Alexandru Pandele**, Mugurel Bălan, M. Piso, Marius Trușculescu, and Claudiu Drăgășanu. 'Pluribus - Nanosatellites Formation'. In: *60th International Astronautical Congress* (2009) (cited on page 35).

[34] **Alexandru Pandele**, Marius Trușculescu, Mugurel Bălan, M. Piso, and Claudiu Drăgășanu. 'Scientific Experiments On Board The Goliat Cubesat'. In: *62nd International Astronautical Congress, Cape Town, South Africa* (2011) (cited on page 36).

[35] Mugurel Bălan, Marius Trușculescu, Claudiu Drăgășanu, **Alexandru Pandele**, and M. Piso. 'Past, Present And Future Of The Romanian Nanosatellites Program'. In: *62nd International Astronautical Congress* (2011), pp. 1–5 (cited on page 36).